

THESIS FOR THE DEGREE OF DOCTOR OF PHILOSOPHY

mm-Wave Data Transmission and
Measurement Techniques:
A Holistic Approach

DHECHA NOPCHINDA



CHALMERS

Microwave Electronics Laboratory
Department of Microtechnology and Nanoscience – MC2
Chalmers University of Technology
Gothenburg, Sweden, 2019

mm-Wave Data Transmission and Measurement Techniques: A Holistic Approach

DHECHA NOPCHINDA

ISBN 978-91-7905-201-0

© Dhecha Nopchinda, 2019

Doktorsavhandlingar vid Chalmers tekniska högskola
Ny series nr 4668
ISSN 0346-718X

Chalmers University of Technology
Department of Microtechnology and Nanoscience – MC2
Microwave Electronics Laboratory
SE-412 96 Gothenburg, Sweden
+ 46 (0)31-772 1000

Printed by Chalmers Reproservice
Gothenburg, Sweden 2019

“Mr. Watson, come here — I want to see you...”

Alexander Graham Bell, 1876.

Abstract

The ever-increasing demand on data services places unprecedented technical requirements on networks capacity. With wireless systems having significant roles in broadband delivery, innovative approaches to their development are imperative. By leveraging new spectral resources available at millimeter-wave (mm-wave) frequencies, future systems can utilize new signal structures and new system architectures in order to achieve long-term sustainable solutions.

This thesis proposes the holistic development of efficient and cost-effective techniques and systems which make high-speed data transmission at mm-wave feasible. In this paradigm, system designs, signal processing, and measurement techniques work toward a single goal; to achieve satisfactory system level key performance indicators (KPIs). Two intimately-related objectives are simultaneously addressed: the realization of efficient mm-wave data transmission and the development of measurement techniques to enable and assist the design and evaluation of mm-wave circuits.

The standard approach to increase spectral efficiency is to increase the modulation order at the cost of higher transmission power. To improve upon this, a signal structure called spectrally efficient frequency division multiplexing (SEFDM) is utilized. SEFDM adds an additional dimension of continuously tunable spectral efficiency enhancement. Two new variants of SEFDM are implemented and experimentally demonstrated, where both variants are shown to outperform standard signals.

A low-cost low-complexity mm-wave transmitter architecture is proposed and experimentally demonstrated. A simple phase retarder predistorter and a frequency multiplier are utilized to successfully generate spectrally efficient mm-wave signals while simultaneously mitigating various issues found in conventional mm-wave systems.

A measurement technique to characterize circuits and components under antenna array mutual coupling effects is proposed and demonstrated. With minimal setup requirement, the technique effectively and conveniently maps prescribed transmission scenarios to the measurement environment and offers evaluations of the components in terms of relevant KPIs in addition to conventional metrics.

Finally, a technique to estimate transmission and reflection coefficients is proposed and demonstrated. In one variant, the technique enables the coefficients to be estimated using wideband modulated signals, suitable for implementation in measurements performed under real usage scenarios. In another variant, the technique enhances the precision of noisy S-parameter measurements, suitable for characterizations of wideband mm-wave components.

Keywords: Active load pull, coherent optical system, communication system, data transmission experiment, digital signal processing, estimation theory, identification theory, impairment compensation algorithm, linear measurement technique, microwave network analysis, millimeter wave (mm-wave) system, multiplier based transmitter, mutual coupling effects, spectral efficiency, spectrally efficient frequency division multiplexing (SEFDM), vector network analyzer, wideband measurement.

List of Publications

Appended Publications

This thesis is based on the work contained in the following papers:

- [A] **D. Nopchinda**, T. Xu, R. Maher, B. C. Thomsen, and I. Darwazeh, “Dual polarization coherent optical Spectrally Efficient Frequency Division Multiplexing,” *IEEE Photonics Technology Letters*, vol. 28, no. 1, pp. 83–86, Jan. 2016.
- [B] **D. Nopchinda**, Z. He, G. Granstrom, M. Gavell, and H. Zirath, “8-PSK upconverting transmitter using E-band frequency sextupler,” *IEEE Microwave and Wireless Components Letters*, vol. 28, no. 2, pp. 177–179, Feb. 2018.
- [C] **D. Nopchinda**, and K. Buisman, “Measurement technique to emulate signal coupling between power amplifiers,” *IEEE Transactions on Microwave Theory and Techniques*, vol. 66, no. 4, pp. 2034–2046, Apr. 2018.
- [D] H. Ghannam, **D. Nopchinda**, M. Gavell, H. Zirath, and I. Darwazeh, “Experimental demonstration of Spectrally Efficient Frequency Division Multiplexing transmissions at E-band,” *IEEE Transactions on Microwave Theory and Techniques*, vol. 67, no. 5, pp. 1911–1923, May. 2019.
- [E] **D. Nopchinda**, T. Eriksson, H. Zirath, and K. Buisman, “Measurements of reflection and transmission coefficients using finite impulse response least-squares estimation,” accepted for publication in *IEEE Transactions on Microwave Theory and Techniques*.

Other Publications

The content of the following publications partially overlaps with the appended papers or is out of the scope of this thesis.

Journal Papers

- [JP1] Z. He, **D. Nopchinda**, T. Swahn, and H. Zirath, “A 15-Gb/s 8-PSK demodulator with comparator-based carrier synchronization,” *IEEE Transactions on Microwave Theory and Techniques*, vol. 63, no. 8, pp. 2630–2637, Aug. 2015.
- [JP2] S. Carpenter, **D. Nopchinda**, M. Abbasi, Z. S. He, M. Bao, T. Eriksson, and H. Zirath, “A D-Band 48-Gbit/s 64-QAM/QPSK direct-conversion I/Q transceiver chipset,” *IEEE Transactions on Microwave Theory and Techniques*, vol. 64, no. 4, pp. 1285–1296, Apr. 2016.
- [JP3] W. Hallberg, **D. Nopchinda**, C. Fager, and K. Buisman, “Measurement-based Doherty amplifier emulation using a single amplifier,” submitted to *IEEE Microwave and Wireless Components Letters*, 2019.

Conference Papers

- [CP1] **D. Nopchinda**, and K. Buisman, “Emulation of array coupling influence on RF power amplifiers in a measurement setup,” in *Microwave Measurement Conference (ARFTG)*, San Francisco, CA, 2016, pp. 1–4.
- [CP2] O. Habibpour, **D. Nopchinda**, Z. S. He, N. Rorsman, and H. Zirath, “Generation of multi-Gigabit/s OFDM signals at W-band with a Graphene FET MMIC mixer,” in *2017 IEEE MTT-S International Microwave Symposium (IMS 2017)*, Honolulu, HI, 2017, pp. 1185–1187.
- [CP3] **D. Nopchinda**, and K. Buisman, “An active load-Pull technique creating time-variant impedances to emulate coupling between power amplifiers,” in *2017 IEEE MTT-S International Microwave Symposium (IMS 2017)*, Honolulu, HI, 2017, pp. 1437–1440.
- [CP4] **D. Nopchinda**, T. Eriksson, and K. Buisman, “Estimation of load-pull reflection coefficients for modulated signals,” in *2018 IEEE MTT-S International Microwave Symposium (IMS 2018)*, Philadelphia, PA, 2018, pp. 1168–1171.

Thesis

Some of the work presented in this thesis, such as text, figures and tables may be partly or fully reused from the thesis below, which is part of the author’s doctoral studies, without being explicitly stated.

D. Nopchinda, “Digital techniques for high data-rate communication at millimeter-wave,” Tekn. Lic. Thesis, Dept. of Microtechnology and Nanoscience, Chalmers University of Technology, 2017.

Patent

D. Nopchinda, and K. Buisman, “Method and systems for network analysis,” SE Patent App. 1850697-2, 2018.

Previous Work

The following existing work is not part of the author’s doctoral studies.

B. Srisuchinwong, and **D. Nopchinda**, “Current-tunable chaotic jerk oscillator,” *Electronics Letters*, vol. 49, no. 9, pp. 587–589, Apr. 2013.

Acronyms

5G	Fifth Generation Mobile Networks
ACPR	Adjacent Channel Power Ratio
AWG	Arbitrary Waveform Generator
AWGN	Additive White Gaussian Noise
BER	Bit-Error Rate
CO	Coherent Optical
CMA	Constant Modulus Algorithm
CPUT	Coupling-Path Under Test
DC	Direct Current
DFT	Discrete Fourier Transform
DP	Dual Polarization
DPD	Digital Pre-Distortion
DSP	Digital Signal Processing
DUT	Device Under Test
EVM	Error-Vector Magnitude
FEC	Forward Error Correction
FFT	Fast Fourier Transform
FIR	Finite Impulse Response
ICI	Inter Carrier Interference
IF	Intermediate Frequency
ILS	Integer Least Square
IP	Internet Protocol
ITU	International Telecommunication Union
KPI	Key Performance Indicator
LDPC	Low-Density Parity-Check
LO	Local Oscillator
LPF	Low-Pass Filter
LS	Least-Squares
LSE	Least-Squares Estimation
ML	Maximum Likelihood
MIMO	Multiple-Input Multiple-Output
MZM	Mach-Zehnder Modulator
NMSE	Normalized Mean-Square Error

OFDM	Orthogonal Frequency Division Multiplexing
OPU	Offline Processing Unit
OSNR	Optical Signal-to-noise Ratio
PA	Power Amplifier
PDF	Probability Density Function
PDM	Polarization Division Multiplexing
PMD	Polarization Mode Dispersion
PSD	Power Spectral Density
PSK	Phase-Shift Keying
QAM	Quadrature Amplitude Modulation
QPSK	Quadrature Phase-Shift Keying
RF	Radio Frequency
RS	Reed-Solomon
RX	Receiver
SD	Sphere Decoder
SDR	Software-Defined Radio
SEFDM	Spectrally Efficient Frequency Division Multiplexing
SNR	Signal-to-Noise Ratio
TPUT	Transmission-Path Under Test
TX	Transmitter
TS	Training Sequence
VNA	Vector Network Analyzer
ZF	Zero-Forcing

Contents

Abstract	v
List of Publications	vii
Acronyms	xi
1 Introduction	1
1.1 Towards mm-Wave Wireless	1
1.2 Current Development of Wireless Communication Systems . . .	4
1.3 Holistic Approach to Development of Next Generation mm-Wave Systems	4
1.3.1 Data Transmission (Digital)	6
1.3.2 Measurement Techniques (Analog)	6
1.4 Novelty and Outline	8
2 Spectrally Efficient Frequency Division Multiplexing	11
2.1 Overview of SEFDM	11
2.1.1 Theoretical Description	11
2.1.2 Comparison between OFDM and SEFDM	12
2.2 Mitigation of ICI in SEFDM Systems	14
2.2.1 Decoders	14
2.2.2 Forward Error Correction	17
2.3 SEFDM Impairment Compensation	18
2.3.1 Conventional Impairment Correction Techniques and Their Incompatibility with SEFDM Systems	18
2.3.2 Polarization MIMO Equalizer	19
2.3.3 Frequency Offset and Phase Noise Compensation	22
2.4 Practical Considerations	24
3 Frequency Multiplier-Based Transmitter	27
3.1 mm-Wave Signal Generation	27
3.2 Multiplier-Based Transmitters	28
3.2.1 Frequency Multiplier Nonlinear Model	29
3.2.2 Output Impairments	30
3.2.3 Existing Approaches	30
3.3 Upconverting Transmitter Using Frequency Multiplier Coupled with Phase Retarder	31
3.3.1 Phase Retarder	31

3.3.2	Compensated Nonlinearity	32
3.4	Digital Receiver	33
3.4.1	Post-Distorter	33
3.4.2	Phase Error Compensator	34
4	Emulation of Mutual Coupling for Characterization and Evaluation Measurements	37
4.1	Brief Overview	38
4.2	Antenna Array Applications for Communication	38
4.3	Antenna Array Output Coupling	39
4.4	Emulation Method	40
4.4.1	Overview	40
4.4.2	Offline Processing Unit	41
4.4.3	Measurement Setup	42
4.4.4	Isolation of Coupling Effects	43
4.4.5	Calibration	48
4.5	Applications	48
5	A Technique to Measure Reflection and Transmission Coefficients	51
5.1	Applications of Transmission and Reflection Coefficients	51
5.1.1	Vector Network Analyzers: S-Parameters	52
5.1.2	Active Load-Pull: Load Relection Coefficients	53
5.2	Measurement	54
5.2.1	Setup (Framework)	54
5.2.2	Definition-Based Approach	55
5.3	Finite Impulse Response Least-Squares Approach	57
5.3.1	FIR-LSE Variant I (Time-Time)	57
5.3.2	FIR-LSE Variant II (Time-Frequency)	59
5.3.3	FIR-LSE Variant III (Frequency-Frequency)	60
5.4	Applications	62
6	Conclusions	63
6.1	Contributions	63
6.2	Future Directions	65
	Acknowledgments	67
	Bibliography	71

Chapter 1

Introduction

Communication system has been at the forefront of technological developments in the past century. From warfare and space exploration to Internet-connected laundry machine, it is our humanly desires to be involved, to control, to be entertained, to communicate that drive the advancement of these systems forward. Yet, in the time of instantaneous connections at a finger tip, there is more to be done.

In 2019, just shy of 30 years after the World Wide Web became public, almost 6 out of 10 of the global population have access to the Internet, a proportion which grew more than eleven-fold in 19 years [1]. For perspective, the world’s population itself increased by less than 26% [2]. Cisco [3] predicts that in the year 2022, a not so distant future, the annual global Internet Protocol (IP) traffic will be 4.8 zettabytes, resulting in projected monthly IP traffic per global capita of 50 GB. Platform-wise, smartphones are projected to occupy almost half of the traffic, while personal computers will account for less than 20% of the data being transmitted. The number of “connected devices” will be more than triple the human population. Application-wise, a 2018 report [4] shows that video-streaming represents the highest global traffic-share, occupying more than half of the aggregated downstream traffic, while web-browsing itself represents less than 20% of the downstream. The question whether the shift in consumer demands pushes the technological advancement, or the advancement enables the demands, is of less importance. It is, however, important to acknowledge the ever-increasing demand on data services, which places unprecedented technical requirements on network capacity, both at the core and access networks. With wireless systems being at the heart of broadband delivery, innovative approaches to their design and development are in great need. Traditional coding and modulation design approaches need to be reconsidered, and new regions of the spectrum need to be allocated. Future systems will require new spectral resources, new signal structures, and new system designs.

1.1 Towards mm-Wave Wireless

To address the data capacity challenges imposed on mobile networks, a two-pronged approach is typically used. Firstly, spectral efficiency is increased,

commonly done by increasing the modulation order, i.e., encoding more bits in a data symbol, but at the cost of higher transmission power. Secondly, the transmitting signal is upconverted to higher radio frequencies (RF), which support wider bandwidths.

Microwave systems are commonly found to operate at subsets of the highly-congested frequency range from 1 to 28 GHz. Therefore, millimetre-wave (mm-wave) systems, which operate at higher frequencies within 30 to 300 GHz, have received significant interests from both academia and industries. For 5G, which is expected to handle more than one-tenth of the global mobile traffic by 2022 [3], the E-band frequency range, through its wider available bandwidth (combining 71–76 GHz with 81–86 GHz), has become an important candidate for both access and backhaul systems [5–7]. Ericsson, in its 2018 report [8], predicts that by 2023, 40% of the global backhaul connections will be wireless, a figure which rises to 65% if North East Asia, which has disproportionately large fiber penetration, is excluded. E-band is expected to provide hop-length up to 3 km and is now being used for up to 20% of the backhaul hops in some countries.

The strategy of increasing the center frequency in search of an unoccupied spectrum and wider bandwidths has proven to be effective over the years and will be applied in the future as recent successful demonstrations at frequencies higher-than-E-band have been achieved, e.g., the recent pioneering work in D-band (130–175 GHz) —**Paper JP2**— and W-band (75–110 GHz) —**Paper CP2**—. Nevertheless, in order to create a long-term sustainable cost-effective system, the optimization and utilization efficiencies of these frequencies need to be considered at all design-stages from the circuits to the whole system.

In terms of research, mm-wave is of important interest as unique impairments and effects, negligible at lower frequencies start to appear. At the circuit and sub-system level, commonly used approaches for interconnects and packaging of circuits become inappropriate, e.g., bond-wiring exhibits severely inductive behaviour and poor performance [9]. At the system level, the white phase noise of oscillators, typically neglected at lower frequencies, has become more detrimental to the signal quality than the near-carrier phase noise due to the wider signal bandwidths [10].

Current wireless systems transmit standard signals, e.g., quadrature phase-shift keying (QPSK). To increase spectral efficiency, the modulation order is typically increased, e.g., from QPSK to 16-quadrature amplitude modulation (QAM), which doubles the spectral efficiency. Fig. 1.1 shows the resulting spectral efficiency at a given modulation order (constellation size), along with the corresponding signal-to-noise ratio (SNR)-per-bit required for the bit-error rate (BER) of 10^{-6} in an additive white Gaussian noise (AWGN) channel. It can be seen that the spectral efficiency increases with the modulation order but at the cost of higher SNR requirement, and hence, the transmitted power. This approach, while standard, is severely limited at mm-wave frequencies. This is mainly due to the limited output power, the stronger attenuation during transmission as shown in Fig. 1.2 and 1.3, and the higher phase noise of frequency-multiplied oscillator signals [11]. The higher linearity requirement of standard spectrally efficient signals coupled with unique impairments found at such frequencies further exacerbate the constraints [12].

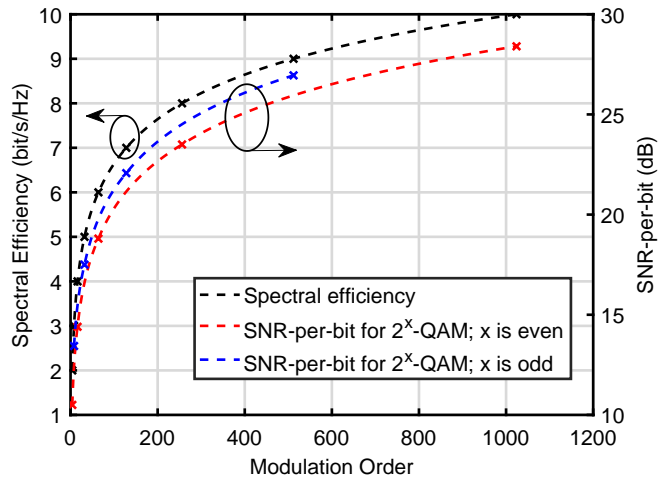


Figure 1.1. Spectral efficiency and SNR-per-bit vs modulation order (constellation size).

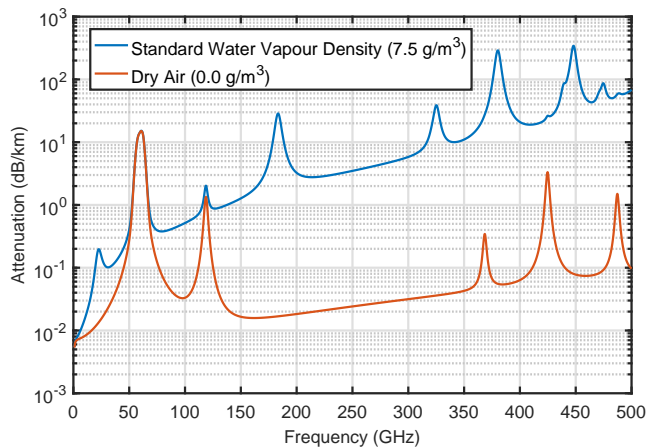


Figure 1.2. Atmospheric attenuation up to 500 GHz calculated using ITU atmospheric gas attenuation model at the mean annual global reference atmosphere (1013.25 hPa and 15°C) [13].

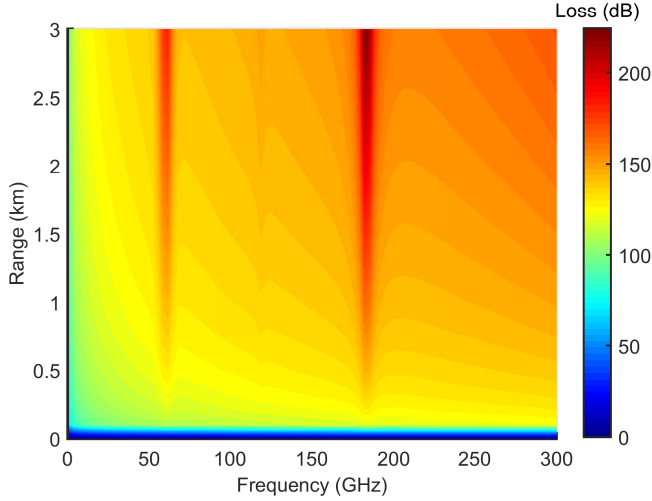


Figure 1.3. Combined free-space path loss and atmospheric attenuation (7.5 g/m^3 , 1013.25 hPa , and 15°C).

1.2 Current Development of Wireless Communication Systems

The development of wireless communication systems, shown in Fig. 1.4, is traditionally structured as non-interactive non-cross disciplinary discrete work packages. The structure is simplified and shown in Fig. 1.5. Circuit designers optimize their designs of the analog transmitter (TX) and receiver (RX) according to conventional metrics, e.g., output power, distortion, bandwidth, noise factor, and stability. Measurements of these circuits and components are done using standard signals, typically frequency swept sinusoids, which do not represent digital and wideband signals found in real usage scenarios. Considerations of key performance indicators (KPIs), including BER, error-vector magnitude (EVM), data rate, and spectral and energy efficiencies, currently come at the final-stage, after generic signal generations and generic digital signal processing (DSP) algorithms have been integrated to the digital TX and RX. Satisfactory KPIs of the system as a whole are expected through succession, not optimization. This fact implies that the analog TX and RX are not designed to optimize the final performance, and simultaneously, the digital TX and RX are not designed to take advantage of the available performance in the analog chains; the results are poor utilization efficiency and low cost-effectiveness.

1.3 Holistic Approach to Development of Next Generation mm-Wave Systems

In order to lay the foundations for joint optimizations of the main constituents of next generation mm-wave systems, this thesis proposes a cross-disciplinary holistic paradigm, where microwave techniques, used at circuit and sub-system

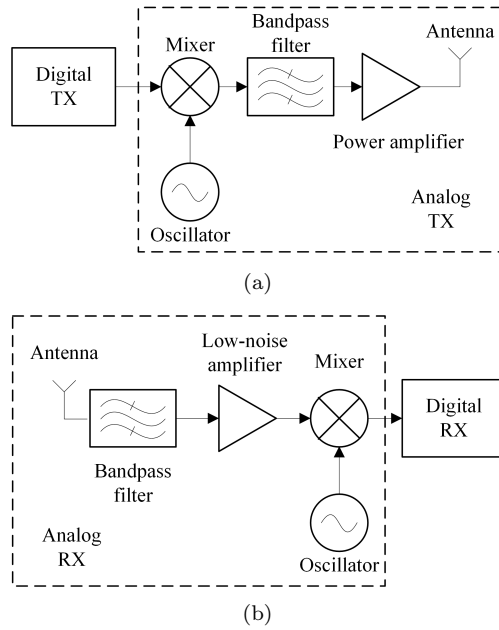


Figure 1.4. Simplified block-diagram of a wireless communication system: (a) transmitter, and (b) receiver.

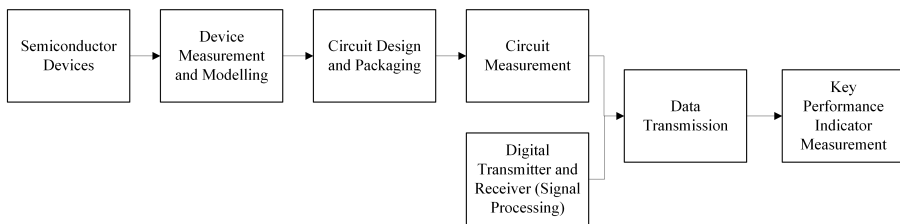


Figure 1.5. Current approach to develop wireless communication systems.

levels, are cross-pollinated with system-level methods of signal processing. Conceptually, the proposed paradigm maybe divided into two intimately related parts: data transmission (digital) and measurement techniques (analog).

1.3.1 Data Transmission (Digital)

Within the digital TX and RX, signals and DSP algorithms are conventionally designed using isolated behavioral models. For example, a frequency offset compensation algorithm is commonly designed and derived in a model with only AWGN and frequency offset. However, such assumption of isolated events and effects rarely holds true in practice where all impairments, e.g., thermal and phase noise, frequency offset, time delay, channel response, and interference, are intertwined. This mismatch between development and deployment results in impeded efficacy of the system. This thesis recognizes the pragmatic need to develop signals and DSP algorithms in conjunction, which are subsequently demonstrated experimentally.

To optimize the trade-off between spectral efficiency and power, which is especially important at mm-wave frequencies, this thesis presents experimental implementations and demonstrations of specially designed signals and DSP algorithms. The pairing allows for continuous tuning and optimization of the spectral efficiency—Spectrally Efficient Frequency Division Multiplexing (SEFDM). SEFDM is a multi-carrier signal, first proposed in [14], which allows for two dimensions of spectral efficiency enhancement: discretely at the symbol-level and continuously at the carrier-level. **In Paper A, SEFDM coupled with the sphere decoder (SD) [15] were implemented and demonstrated for the first time in a coherent optical system, where transmissions over 80 km have been successfully performed.** The work in Paper A laid the foundation for subsequent implementation in mm-wave systems. For 5G, forward error corrections (FEC) using low-density parity-check (LDPC) codes, invented by Gallager in 1962 [16], have been adopted in future standards [17]. **In Paper D, SEFDM coupled with LDPC codes were implemented in a mm-wave experimental test bed, being the first-ever demonstration of SEFDM at E-band.** In both scenarios, it has been shown that SEFDM outperforms standard signals in spectral efficiency.

To generate mm-wave oscillator signals, a common approach is to frequency-multiply lower frequency sources. It is believed that such approach would achieve better performance and design accuracy [18], or better stability and phase noise [19]. However, mixing wideband baseband or intermediate frequency (IF) signals with mm-wave frequency-multiplied oscillator signal results in the so called “multiplicative noise” which scales with the signal power [12]. **Instead of using mixers and oscillators, this thesis presents a method to upconvert IF signals using only a frequency multiplier in Paper B.**

1.3.2 Measurement Techniques (Analog)

Circuits and sub-systems measurement techniques and apparatuses conventionally follow incumbent standard practices dictated by specific evaluation criteria and constraints rather than actual end-user applications. These instruments, albeit with some exceptions, use generic sinusoid(s) signals as stimuli instead of

wide-band modulated signals found in real usage scenarios, as they are designed to measure conventional metrics instead of the KPIs. Standard instruments do not perform direct characterization of the components under the transmission environment without cumbersome mapping procedure to the measurement environment. Yet, the results of these measurements are critically important and are used by designers to make informed design decisions of the circuits, sub-systems, and integration thereof.

As mm-wave devices, components, circuits, and sub-systems are connected and integrated, they interact with each other both linearly and nonlinearly. This means that even if the characterization of each component reveals satisfactory performance with conventional metrics, the situation could change significantly after integration. Such interaction is complex; circuit simulation tools, e.g., harmonics balance and time-domain, often cannot reveal these nuances in integrated systems due to the associated complexity cost. Complete electromagnetic simulations are typically performed exclusively on passive components, which merely serve as pass-or-fail tolerance tests. The issue is further exacerbated by the modelling inaccuracies of semiconductor devices which support mm-wave frequencies. Finally, in multi-antenna environment, the standard practice of matching to 50-Ohm is less applicable due to mutual coupling effects [20], which cause variations of the load-reflection coefficients at various points in the system. Yet, circuit designers have the difficult task of locating and improving upon the limiting component in mm-wave systems. Such task is non-trivial as even with the costly prototype fabricated, it is the accumulation of effects and impairments that are observed. This issue is directly measurement-related; new characterization techniques and metrics must be developed.

As the transmission scenarios of next generation systems are increasingly complex; to assist and enable hardware designs, which are optimized under real usage scenarios, new measurement systems with the capabilities to characterize components under transmission environments and visualize the resulting effects on the KPIs must be developed. Such measurement technique would allow circuit designers to have access to system-level performance metrics and KPIs with only part of the prototype systems fabricated, ultimately reducing cost and time. A new measurement technique of such nature, first proposed by the author in **Papers CP1 and CP3**, is presented in this thesis in **Paper C. The technique, which is based on active load-pull [21], enables power amplifier (PA) designers to obtain the resulting KPIs when the PAs are integrated into complex multi-antenna transmission environments**, such as beamforming and Massive MIMO arrays, while requiring only one PA to be realized and fabricated.

Complementary to the technique in Paper C, **the work in Paper E presents a method to measure and estimate reflection coefficients in active load-pull systems when the incident and reflected waves are wide-band modulated signals**. The method is also applicable in wideband S-parameter measurements with a vector network analyzer (VNA). The technique solves the problems and the difficulty associated with the estimation of load reflection coefficients in the former scenario and improves the precision of measured S-parameters in the latter.

1.4 Novelty and Outline

This thesis is a result of inter-disciplinary efforts to introduce a new paradigm in the development of wireless communication systems. Ultimately, the goal is to lay the foundations necessary to realize mm-wave system that is both fast and efficient, which can be expressed as follows:

Objective I, efficient mm-wave data transmission, deals with the practical design and experimental demonstration of spectrally-efficient signals and impairment correction algorithms suitable for mm-wave transmission. Research activities addressing various issues of mm-wave data transmission are in abundant. Most of the activities can be categorized as follows: theoretical system-level communication techniques, which have not been experimentally demonstrated with working mm-wave transceivers [22–25], and practical analog system integration and designs which have been demonstrated using standard basic communication and DSP techniques, more suitable at lower frequencies [26–33]. There exists a gap for research efforts combining the two realms, where advance communication and DSP techniques are integrated with advance mm-wave analog TX and RX. The objective addresses this through experimental demonstrations of the efficiency, performance, and practicability of signals with working mm-wave transceivers. Two different signals are fully demonstrated in this thesis: SEFDM, which enhances spectral efficiency, and phase-retarded M-PSK, which enables low-cost low-complexity multiplier-based upconversion of data signal to mm-wave frequencies. **Digital deliverables:**

- Paper A experimentally demonstrates SEFDM coupled with SD in a dual-polarization coherent optical system over 80 km of single mode fiber, which laid the basis for the subsequent experimental demonstration of SEFDM coupled with LDPC at E-band in Paper D. The discussion on SEFDM continues in **Chapter 2**.
- Paper B proposes and experimentally demonstrates a phase retarder predistorter, which enables low-cost upconversion and transmission using E-band frequency multiplier. Multiplier-based TX is covered in **Chapter 3**.
- Papers CP2 and JP2 present experimental transmission demonstrations of standard signals at W-band and D-band, respectively, and are not included in the thesis.
- Paper JP1 presents a technique to generate the local oscillator signal at the RX from the received RF signal. The technique is not discussed further in this thesis.

Objective II, measurement techniques to enable and assist the design and evaluation of mm-wave circuits, aims to realize measurement techniques which would perform device under test (DUT) characterization under real usage scenarios. The objective evaluates the performance in the *forward direction*, i.e., if the impairment is known, how would the KPIs be affected. Existing works in this area at mm-wave are based on behavioral expressions and have some levels of simplification. The analytical technique, which uses EVM as the KPI, proposed by Antes and Kallfass [11] is an important

milestone in this area: the technique considers AWGN, I/Q imbalance, phase noise and DC offsets, contributed by various components, but forgoes PA and any associated nonlinearity. Similarly, Santos and Carvalho [34] studied the perturbation of EVM under PA distortion, while Khanzadi *et al.* [10] derived the EVM bound when the signal is impaired by phase noise. In contrast to these, we build measurement systems with the ability to emulate mm-wave real usage scenarios to characterize the DUT and measure the resulting KPIs including EVM and BER. Due to the spectral and energy efficiencies offered by Massive MIMO [35], further supported by the smaller array size at mm-waves, we have built a measurement system with the capability to characterize DUTs under mm-wave Massive MIMO scenarios. **Analog deliverables:**

- Paper C presents a measurement technique to emulate mutual coupling effects in order to characterize PAs in antenna array transmission scenarios. The technique enables system-level evaluation in terms of relevant performance metrics and KPIs under both beamforming and Massive MIMO applications, while requiring only one PA to be fabricated. The technique is further discussed in **Chapter 4**.
- Paper E presents a measurement technique to estimate the transmission and reflection coefficients. When applied to S-parameter measurements with vector network analyzers, the technique offers precision improvements. The technique is also capable of estimating the coefficients when the incident and reflected waves are wideband modulated signals, found in some active load-pull applications. The discussion continues in **Chapter 5**.
- Papers CP1 and CP3 are the foundations of Paper C and are not included in this thesis.
- Paper CP4 is the basis of Paper E and is not included in this thesis.
- Paper JP3 presents an extension and modification of the emulation technique, presented in Paper C, to study and evaluate Doherty PAs and is not included in this thesis.

The thesis is concluded in **Chapter 6**.

Chapter 2

Spectrally Efficient Frequency Division Multiplexing

In this chapter, a special signal with continuously-tunable enhanced spectral efficiency called Spectrally Efficient Frequency Division Multiplexing (SEFDM) is presented. SEFDM and the developed signal processing techniques are experimentally demonstrated in Papers A and D. SEFDM is a multicarrier modulation format [36], similar in construction to Orthogonal Frequency Division Multiplexing (OFDM) [37]. However, unlike OFDM, the uniform frequency spacing between each adjacent subcarriers is not the inverse of the uniform subcarrier symbol rate, but are scaled by a real parameter, $\alpha \in [0, 1]$. Assuming that in a symbol period each subcarrier is carrying a complex symbol, the subcarriers in SEFDM will be orthogonal if and only if α is unity. In this instance, SEFDM is also equivalent to OFDM. Otherwise, for a positive α less than unity, the subcarrier spacing is less than that required to maintain subcarrier orthogonality, which effectively “compresses” the bandwidth required to transmit at given data rate. The real-time adjustable [38] non-orthogonal subcarrier spacing then introduces inter carrier interference (ICI). Hence, through α , SEFDM creates a continuously-tunable and directly optimizable (capable of being optimized) trade-off between spectral efficiency, transmit power, and receiver complexity [39].

2.1 Overview of SEFDM

2.1.1 Theoretical Description

The transmitting serial stream of data symbols, e.g. QPSK, 8-QAM, and 16-QAM, are separated into multiple parallel streams. In particular, for N number of subcarriers, the symbols are sorted into N parallel streams. Each symbol stream is then modulated onto the corresponding subcarrier. The modulated streams at different frequencies are then superimposed in time resulting in

SEFDM baseband signal, $x(t)$, which can be represented as

$$x(t) = \frac{1}{\sqrt{T}} \sum_{l=-\infty}^{\infty} \sum_{n=0}^{N-1} s_{l,n} \exp \left[\frac{j2\pi n\alpha(t-lT)}{T} \right], \quad (2.1)$$

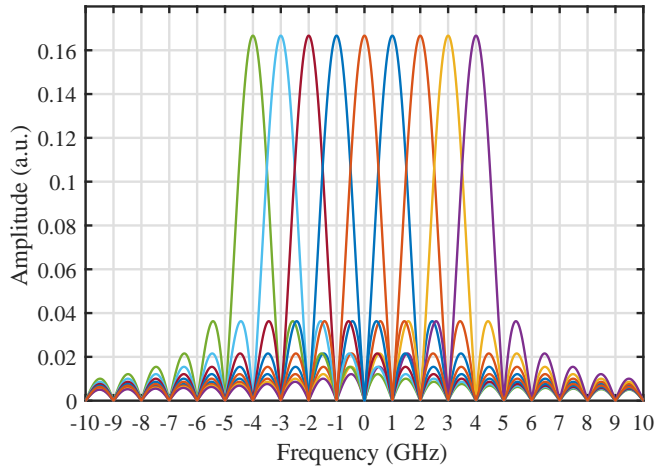
where j is $\sqrt{-1}$ and $s_{l,n}$ is the complex data symbol of the n^{th} subcarrier and the l^{th} SEFDM symbol with period T . For clarity, $n \in \{0, 1, 2, \dots, N-1\}$ and $l \in \{-\infty, \dots, -2, -1, 0, 1, 2, \dots, \infty\}$. The parameter α is the tunable bandwidth compression factor, defined as $\alpha = \Delta F \cdot T$, where ΔF is the uniform frequency spacing between two adjacent subcarriers in Hz. With α of unity, (2.1) represents an OFDM baseband signal. It may also be important to note that the indexing of n is arbitrary and can be implemented in other forms, e.g., $n \in \{-\frac{N}{2}, -\frac{N}{2} + 1, \dots, -2, -1, 0, 1, 2, \dots, \frac{N}{2} - 2, \frac{N}{2} - 1\}$, which does not affect the context of the following discussions. Readers interested in hardware implementations of SEFDM transmitters are referred to [38, 40].

2.1.2 Comparison between OFDM and SEFDM

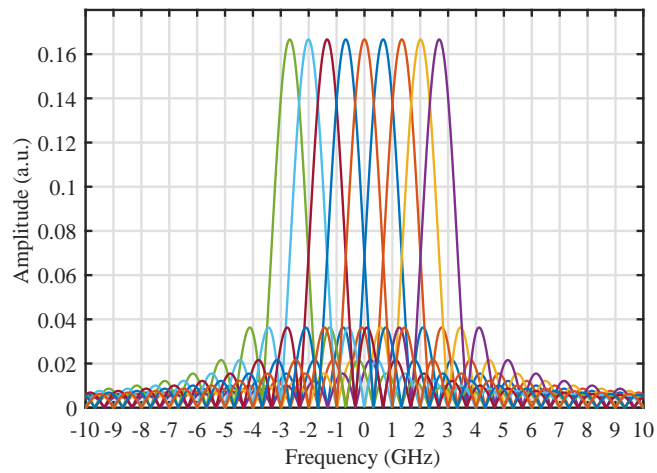
OFDM is a well-known incumbent multicarrier transmission technique, which has been implemented in multiple wireless communication standards, including, IEEE 802.11a [41] and IEEE 802.16b [42]. Its popularity is mainly due to the higher resilience to multipath fading environments [43–45]. For optical transmission, this characteristic transforms to resilience to chromatic dispersion and polarization mode dispersion (PMD) [46–48]. SEFDM, on the other hand, has the advantage of improved spectral efficiency and is proposed as a viable solution for next generation systems [49, 50] at mm-wave [51]. Given OFDM popularity, in combination with the multicarrier nature of SEFDM, comparison between the two is of interest.

While ICI is introduced in SEFDM, its main benefit is the bandwidth compression characteristic. In an example scenario: QPSK symbols are being transmitted at the rate of 9 GBd, i.e., 18 Gbit/s, through 9 subcarriers. Fig. 2.1 shows the frequency allocations of OFDM and SEFDM with α of 0.67. This seemingly random choice of α carries an implication as it increases the original spectral efficiency of 2 bit/s/Hz to 3 bit/s/Hz, which is the same increment as changing from QPSK to 8-QAM. In OFDM case, the 3-dB bandwidth is approximately its data symbol rate [44]; in this example, the QPSK rate of 9 GBd results in 9 GHz 3-dB bandwidth as can be observed in Fig. 2.1(a). This results in OFDM spectral efficiency equivalent to the modulation of the symbol it is carrying in this case the 2 bit/s/Hz of QPSK. In other words, OFDM only has one dimension of spectral efficiency adjustments. On the other hand, SEFDM at the same transmission rate and α of 0.67, the 3-dB bandwidth is reduced to 0.67 times that of OFDM, which is 6 GHz as shown in Fig. 2.1(b). It can be observed that in contrast to OFDM, SEFDM provides an additional dimension of spectral efficiency tuning.

Further observation of Fig. 2.1 reveals that the OFDM subcarriers in Fig. 2.1(a) are orthogonal to each other in frequency domain since the peaks of all subcarriers align with the zeros of other subcarriers. The same cannot be observed with SEFDM subcarriers in Fig. 2.1(b). Due to compression, the subcarriers are not orthogonal to each other and introduces ICI, which will



(a)



(b)

Figure 2.1. Frequency allocations with QPSK symbol rate of 9 GBd carried by 9 subcarriers: (a) OFDM and (b) SEFDM with α of 0.67.

be addressed in Section 2.2. It is also worth mentioning that the introduced ICI also creates practical complications in terms of impairment correction techniques, where standard techniques used with OFDM are not applicable including channel equalization and frequency offset, phase noise, and phase offset compensation techniques. These complications and the developed techniques to mitigate these practicalities will be discussed in Sections 2.3 and 2.4.

2.2 Mitigation of ICI in SEFDM Systems

The benefit of enhanced spectral efficiency in SEFDM comes at the price of ICI, which can pose a detrimental effect to the quality of the received symbols. To mitigate this, three variants of SEFDM systems are established: with decoder(s), with forward error correction (FEC), and with non-uniform power allocations. The first variant uses decoders at the RX-end, which rely on the fact that the ICI in SEFDM is generated by design. Hence, the cross-correlations between each subcarrier are deterministic and known. The second variant does not address the ICI directly, but utilizes FEC channel coding to combat the resulting symbol errors. The last variant is out of the scope of this thesis, interested readers are referred to [52, 53].

2.2.1 Decoders

With the knowledge of the cross-correlation between subcarriers, one has the potential to mitigate SEFDM ICI at the RX through a decoder. Multiple research efforts have focused on developing a suitable decoder for SEFDM [15, 54–59] with considerations for receiver complexity [60] and practical hardware implementations [61–65]. Two different decoders, zero-forcing [66] and sphere decoder [15], are described in this thesis within the scope of application in SEFDM systems.

Zero-Forcing

A zero-forcing (ZF) decoder estimates the transmitted symbols, e.g., QPSK, by utilizing the knowledge of the $N \times N$ cross-correlation matrix of the subcarriers, \mathbf{M} . Note that for OFDM, \mathbf{M} is the identity matrix, \mathbf{I}_N . In an additive white Gaussian noise (AWGN) channel, the received symbols can be described as

$$\mathbf{R} = \mathbf{M}\mathbf{S} + \mathbf{W}, \quad (2.2)$$

where \mathbf{S} is an $N \times 1$ vector containing the constrained transmitted symbols in one SEFDM symbol, \mathbf{W} is an $N \times 1$ noise vector, and \mathbf{R} is the $N \times 1$ received unconstrained symbols vector. ZF decoder tries to cancel-out the ICI through the operation

$$\tilde{\mathbf{R}} = \mathbf{M}^+ \mathbf{R}, \quad (2.3)$$

where \cdot^+ is the pseudo-inverse and $\tilde{\mathbf{R}}$ is the decoded unconstrained symbols. However, due to noise, the decoding operation is imperfect; noise is amplified and the signal-to-noise ratio (SNR) is worsened after ZF. This can be seen by using (2.2) in (2.3), giving

$$\tilde{\mathbf{R}} = \mathbf{M}^+ \mathbf{M} \mathbf{S} + \mathbf{M}^+ \mathbf{W}. \quad (2.4)$$

Assuming, merely for illustration, that \mathbf{M} is invertible, then \mathbf{M}^+ is \mathbf{M}^{-1} . Equation (2.4) then simplifies to

$$\tilde{\mathbf{R}} = \mathbf{S} + \mathbf{M}^{-1}\mathbf{W}. \quad (2.5)$$

Equation (2.5) shows the noise amplification effect, which is dependent on the bandwidth compression. Effectively, with ideal inversion, ZF decoder transforms ICI to worsened SNR of each subcarrier.

To visualize, the noise amplification effect of ZF can be seen through the constellation diagrams of \mathbf{R} (before ZF) and $\tilde{\mathbf{R}}$ (after ZF). Shown in Fig. 2.2 and 2.3 are the constellation diagrams of both symbol sets from an SEFDM experiment with 16 subcarriers and SNR of 12 dB and 6 dB, respectively. Observing the higher-SNR case reveals that the received symbols are severely affected by ICI as shown in Fig. 2.2(a). After ZF, as shown in Fig. 2.2(b), the decoded symbols exhibit improvements as ICI is cancelled-out. However, observing the lower-SNR case reveals unsatisfactory results. Comparing the received symbols in Fig. 2.3(a), where the symbols are affected by both noise and ICI, with the ZF decoded symbols in Fig. 2.3(b) demonstrates the unwanted noise amplification effect of ZF. In this instance, the decoded symbols appears worsened compared to the received symbols. This motivates the combination of ZF with an additional stage of decoder.

Sphere Decoder

Sphere decoder (SD) is an extensive topic in its own right, which deserves a proper investigation. In this thesis, SD will only be discussed within the relevant scope to the experiments. Readers interested in the general description and applications of SD are referred to [67, 68].

The Maximum Likelihood (ML) estimation of the transmitted SEFDM symbols is an Integer Least Square (ILS) problem, which is known to be non-polynomial hard [69]. For SEFDM, this takes the form [15]

$$\tilde{\mathbf{S}} = \arg \min_{\mathbf{S} \in Q^N} \|\mathbf{R} - \mathbf{MS}\|^2, \quad (2.6)$$

where $\|\cdot\|$ is the Euclidean distance, $\tilde{\mathbf{S}}$ is an $N \times 1$ vector of the SD estimated constrained symbols, and Q is the constrained complex symbol set, e.g., the four QPSK symbols and the sixteen 16-QAM symbols. Solving (2.6) will give the optimum solution to the transmitted SEFDM symbols, albeit with very high complexity since it has to consider Q^N solutions for every SEFDM symbol. On the other hand, SD has been proposed as an alternative which can achieve ML performance but with less complexity [68, 70]. It does this by limiting the number of candidate solutions to be within a hyper-sphere and can be expressed as

$$\tilde{\mathbf{S}} = \arg \min_{\mathbf{S} \in Q^N} \|\mathbf{R} - \mathbf{MS}\|^2 \leq C, \quad (2.7)$$

where C is the hyper-sphere radius defined by the ZF solutions and the SNR [15]. In effect, the number of solutions SD has to consider is less than that of ML, which in turn, reduces the complexity. The number of operations is found to be roughly polynomial in N under high SNR [68].

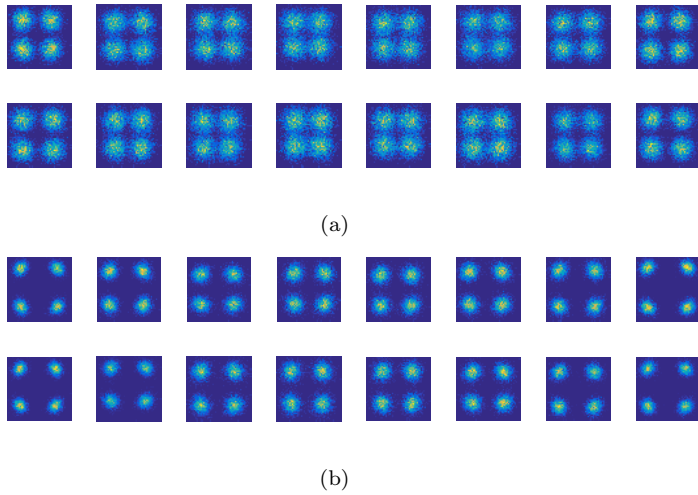


Figure 2.2. Constellation diagrams of SEFDM from an experiment with 16 subcarriers, α of 0.8 and SNR of 12 dB: (a) received symbols, \mathbf{R} , and (b) ZF decoded symbols, $\tilde{\mathbf{R}}$.

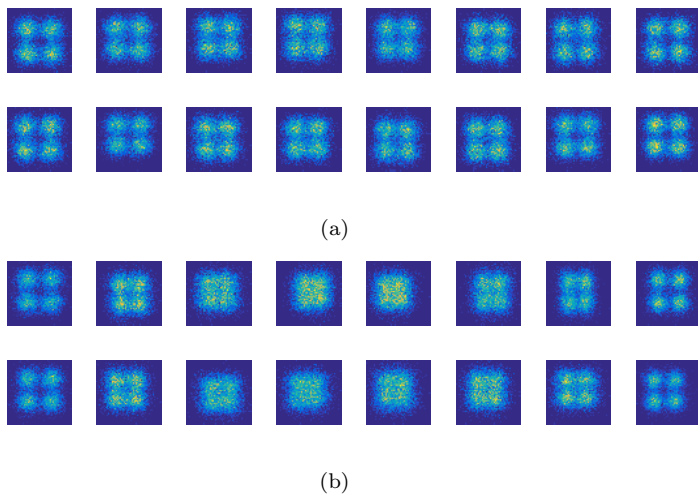


Figure 2.3. Constellation diagrams of SEFDM from an experiment with 16 subcarriers, α of 0.8 and SNR of 6 dB: (a) received symbols, \mathbf{R} , and (b) ZF decoded symbols, $\tilde{\mathbf{R}}$.

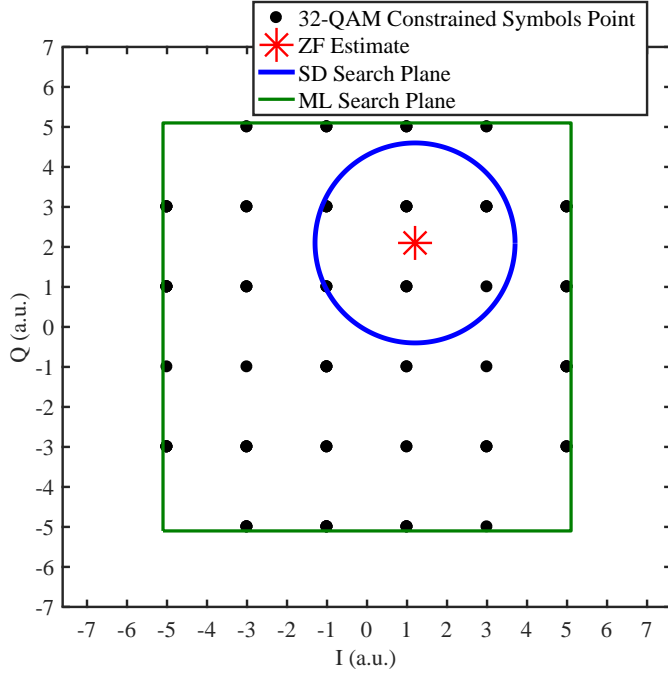


Figure 2.4. Illustration of ML and SD search planes in one SEFDM subcarrier given 32-QAM symbols. In practice, N subcarriers are searched simultaneously, the SD search plane then becomes a hyper-sphere.

The difference between ML and SD operations are illustrated in Fig. 2.4 for one SEFDM subcarrier. As observed in the illustration, the SD search plane is centered around the ZF solution from (2.4). The radius of the search plane is a function of the inverse of the SNR of the channel as described in [15]. It is important to note that the illustration is an over-simplification of the operations, since in practice, N subcarriers are simultaneously searched.

2.2.2 Forward Error Correction

Instead of utilizing decoders, another approach is to indirectly address the ICI through FEC. This is an appealing alternative as it removes one of the fundamental issues of SEFDM systems; the complexity associated with the decoders in SEFDM receivers. Further, the implementations of FEC in cellular systems are widespread and well-known, which would support the adoption of SEFDM for next generation systems.

FEC channel coding was first presented as a viable solution in SEFDM systems in [59], which proposed an implementation of iterative turbo equalizer detector. This is followed by experimental demonstrations and modifications presented and proposed in [50, 51, 71]. Various SEFDM implementations of FEC codes at different code rates including recursive systematic convolutional code, Reed-Solomon (RS), turbo code, and serial concatenations of RS with turbo code are all studied and summarized in [72]. Additionally, a combination

of FEC with serial interference canceller has also been proposed in [73].

To minimize complexity and ultimately demonstrate the practicability of SEFDM at mm-wave, the experiments reported in Paper D used standard low-density parity-check (LDPC) FEC codes [16], which has been adopted in 5G cellular standards [17].

2.3 SEFDM Impairment Compensation

Standard impairment compensation algorithms, e.g., frequency offset compensation, used in OFDM systems are not directly applicable in SEFDM systems due to the following:

1. The ICI between the subcarriers “interferes” or restricts the operation of standard algorithms, which were not developed under ICI conditions.
2. Implementation of standard algorithms after decoding (removal of ICI) is not feasible because the decoders also require that impairments are compensated prior to their operations, i.e., the decoders assume an AWGN channel.

This section considers the practical problems which occur during transmission. This includes frequency offset, phase noise, constant phase offset, polarization rotation (cross-talks between the two polarizations), and PMD. The following discussions are relevant to both the coherent optical system in Paper A and the mm-wave system in Paper D.

2.3.1 Conventional Impairment Correction Techniques and Their Incompatibility with SEFDM Systems

In conventional dual-polarization coherent systems, such as the optical systems described in [74] and demonstrated in [75], the effects of polarization rotation and PMD are mitigated using adaptive linear equalizers. Specifically, constant modulus algorithm (CMA) is used to adapt the taps of the 2×2 MIMO equalizer. To compensate frequency offsets, Viterbi-Viterbi algorithm [76] is used to strip the received baseband signal of modulation, e.g., QPSK, 8-PSK, and 16-PSK. Through Fast Fourier Transform (FFT), the resulting “tone” is then used to estimate and subsequently compensate the frequency offset [77]. After the received symbols are obtained, Viterbi-Viterbi is used again to estimate the constant phase offset, which is then compensated.

In conventional OFDM systems [78], however, an OFDM training sequence instead of CMA is used to estimate the tap-weight of the 2×2 MIMO equalizer [79]. Furthermore, a frame header is also used to estimate the frequency offset [80]. Phase noise and constant phase offset are solved by setting some OFDM subcarriers as pilots.

For SEFDM, the OFDM training sequence, which utilizes OFDM subcarriers, does not have the same frequency allocation of the subcarriers as SEFDM due to bandwidth compression. Hence, the tap-weight of the 2×2 MIMO equalizer cannot be directly estimated. Frame headers can only estimate the frequency offset up to $\pm \frac{1}{2T}$ Hz [80], where T is the OFDM and SEFDM symbol period from (2.1). This limited range cannot be guaranteed to be sufficient in practice.

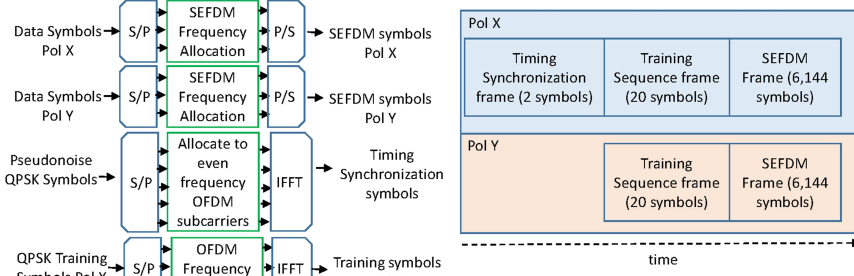


Figure 2.5. Transmission frame structure on both polarizations (Pol X and Pol Y), from Paper A.

Note that this limitation is not exclusive to SEFDM systems. Furthermore, SEFDM subcarriers cannot be used as pilots to estimate both the phase noise and the frequency offset since the pilots will then be perturbed by the ICI.

2.3.2 Polarization MIMO Equalizer

The taps of the 2×2 MIMO equalizer are first estimated using OFDM training sequence (TS) containing 20 OFDM symbols on each polarization (denoted as Pol X and Pol Y for convenience). The TS frame occupies bandwidth less than or equal to that of the following SEFDM data payload, and the frame structure is as shown in Fig. 2.5. The TS frame in each polarization contains 256 OFDM subcarriers, each carrying 20 QPSK symbols.

To utilize the 2×2 MIMO channel, two domains have to be separated. First, the frequency domain determined by the subcarrier frequency allocation. Second, the polarization domain determined by the polarization rotation and PMD at each frequency. At the frequency of each subcarrier, the channel of the polarization domain can be modelled as a 2×2 matrix, denoted as $\mathbf{H}_{OFDM}(n)$, recall that n is the subcarrier index. For clarity, this matrix describes the 2×2 MIMO channel at each frequency. The purpose of the equalizer is to estimate $\mathbf{H}_{OFDM}(n)$ for all n and subsequently remove their effects. In order to do so, a technique developed for MIMO OFDM in mobile wireless channel [81] and adapted for optical channel in [79] is utilized.

The TS symbol sequence of each subcarrier on both polarizations is divided in time into two halves. Each half contains 10 QPSK symbol with a special property. Let the TS frame of the n^{th} subcarrier on both polarizations be denoted by $\mathbf{P}(n)$, which is a 2×20 matrix; the row index denotes polarization (X and Y) and the column index denotes the QPSK symbol in time.

$$\mathbf{P}(n) = \begin{bmatrix} \mathbf{P}_X(n) \\ \mathbf{P}_Y(n) \end{bmatrix} = \begin{bmatrix} \mathbf{A} & \mathbf{A} \\ \mathbf{B} & -\mathbf{B} \end{bmatrix}, \quad (2.8)$$

such that

$$|\mathbf{A}\mathbf{B}^T| = 0,$$

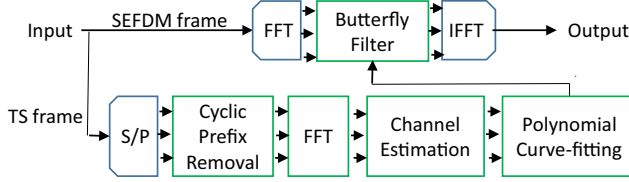


Figure 2.6. Block diagram of the polarization MIMO channel estimation for SEFDM, from Paper A.

and

$$|\mathbf{A}(-\mathbf{B}^T)| = 0,$$

where \cdot^T is the transpose-operation. \mathbf{A} and \mathbf{B} are 1×10 vectors containing QPSK symbols. As imposed in (2.8), the special property of the TS is that each half of the TS on a polarization is orthogonal to the two halves on the other polarization. The received TS frame, $\hat{\mathbf{P}}(n)$, can be described as

$$\hat{\mathbf{P}}(n) = \mathbf{H}_{OFDM}(n)\mathbf{P}(n) + \mathbf{W}(n), \quad (2.9)$$

where $\mathbf{W}(n)$ is the 2×20 AWGN matrix. Using least-squares (LS) estimation, the channel matrix can be estimated as

$$\tilde{\mathbf{H}}_{OFDM}(n) = \hat{\mathbf{P}}(n)\mathbf{P}^+(n) = \mathbf{H}_{OFDM}(n)\mathbf{P}(n)\mathbf{P}^+(n) + \mathbf{W}(n)\mathbf{P}^+(n), \quad (2.10)$$

where $\tilde{\mathbf{H}}_{OFDM}(n)$ is the estimated 2×2 MIMO channel at the n^{th} subcarrier.

With the polarization channel estimated, the problem remains that the estimation corresponds to the OFDM TS frequency allocations not the SEFDM data subcarriers, unless the technique proposed in [82] is used. To solve this, polynomial curve-fitting can be performed to interpolate and extrapolate the estimated OFDM channel to the frequencies of SEFDM subcarriers, giving $\tilde{\mathbf{H}}_{SEFDM}(n)$. This operation is illustrated in Fig. 2.6. The magnitude profile is assumed to be constant over frequency, while the phase is assumed to be dispersion-limited, resulting in a quadratic function over frequency. Fig. 2.7 visualizes the simulated $\tilde{\mathbf{H}}_{SEFDM}(n)$ in comparison to $\tilde{\mathbf{H}}_{OFDM}(n)$ under the described conditions.

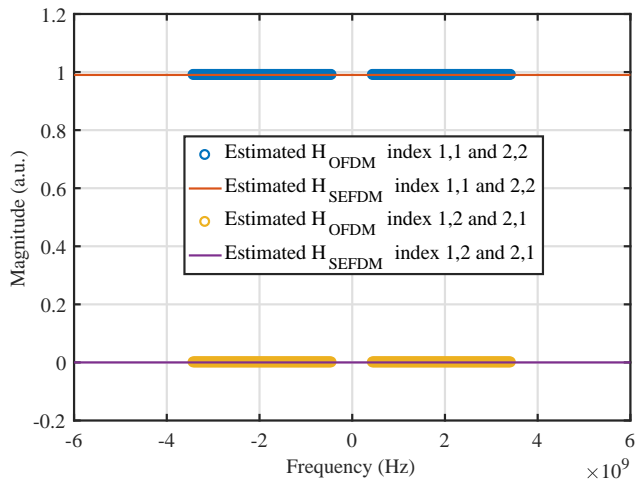
After obtaining $\tilde{\mathbf{H}}_{SEFDM}(n)$, the compensation can be performed on the received SEFDM symbols. Let the number of SEFDM symbols in one polarization be 6,144 to correspond with Fig. 2.5. Denote $\hat{\mathbf{R}}_{SEFDM}(n)$ as a 2×6144 matrix containing the received QPSK symbols on the n^{th} SEFDM subcarrier in both polarizations, described as

$$\hat{\mathbf{R}}_{SEFDM}(n) = \begin{bmatrix} \hat{\mathbf{R}}_X(n) \\ \hat{\mathbf{R}}_Y(n) \end{bmatrix}, \quad (2.11)$$

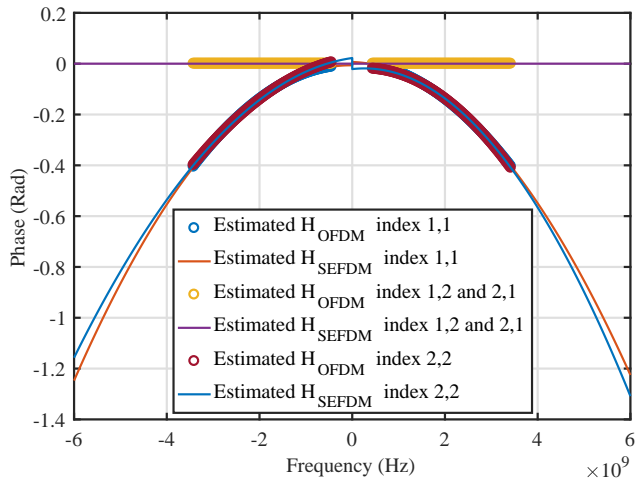
the compensation is then performed as

$$\tilde{\mathbf{R}}_{SEFDM}(n) = \tilde{\mathbf{H}}_{SEFDM}^+(n)\hat{\mathbf{R}}_{SEFDM}(n), \quad (2.12)$$

where $\tilde{\mathbf{R}}_{SEFDM}(n)$ is the polarization-compensated received QPSK symbols. Note that the block diagram in Fig. 2.6 refers to the operation in (2.12) as “butterfly-filtering”.



(a)



(b)

Figure 2.7. Estimated MIMO channel for SEFDM from OFDM training sequence: (a) magnitude and (b) phase.

2.3.3 Frequency Offset and Phase Noise Compensation

A frequency-domain pilot tone can be used to estimate both the frequency offset and phase noise. Such tone can be added specifically or utilized from the leaked oscillator signal at the TX. In the coherent optical system in Paper A, an RF pilot tone can be inserted to the transmitting SEFDM sequence through de-tuning of the Mach-Zehnder modulator (MZM). The same can be achieved by adding a direct current (DC) level to electrical baseband signal in (2.1). The equivalent baseband transmitting signal then becomes

$$x_{tx}(t) = x(t) + c, \quad (2.13)$$

where c is simply a constant to represent DC level. Due to the unintentional difference in frequency (or wavelength) of the lasers or the two oscillators at the TX and RX, the received signal is shifted in frequency, hence, frequency offset, denoted as Δf in Hz. Furthermore, due to the imperfection of both lasers or oscillators, the received signal is further modulated by unwanted random phase variation over time, hence, phase noise, denoted as $\phi(t)$ in rad. By ignoring AWGN, the received signal, $y(t)$, can then be represented as

$$y(t) = x_{tx}(t) \exp[j(2\pi\Delta ft + \phi(t))]. \quad (2.14)$$

Expanding (2.14) with (2.13) gives

$$y(t) = x(t) \exp[j(2\pi\Delta ft + \phi(t))] + c \exp[j(2\pi\Delta ft + \phi(t))]. \quad (2.15)$$

It can be observed that if the received pilot tone, $c \exp[j(2\pi\Delta ft + \phi(t))]$, can be ‘extracted’ from $y(t)$, then Δf and $\phi(t)$ can be estimated. To ease the process of the pilot tone extraction at the receiver, a frequency guard band can be inserted around DC of the baseband signal, $x(t)$. An example of the received signal is shown in Fig. 2.8. Equation (2.15) represents the working model for frequency offset and phase noise estimation and compensation.

At the receiver, an FFT of the received signal, $Y(f)$, is calculated. Due to the narrow-band nature of the pilot tone, the peak of $Y(f)$ corresponds to the frequency location of the pilot tone. Since the pilot should be centered at DC, the estimated frequency of the tone is directly the estimated frequency offset, $\Delta \hat{f}$, [74], i.e.,

$$\Delta \hat{f} = \arg \max_f |Y(f)|. \quad (2.16)$$

Such technique has the following limitations:

1. Frequency resolution of FFT defined as $\frac{f_s}{N_{FFT}}$ Hz, where f_s is the sampling rate in Hz, and N_{FFT} is the number of samples into the FFT, assumed to be the number of the samples of the received signal. This limits the accuracy of the estimation as the frequency offset cannot be guaranteed to be integer-multiple of $\frac{f_s}{N_{FFT}}$.
2. The range of frequency offset must be confined to $\pm \frac{f_s}{2}$ Hz.

Techniques have been developed to ease the former limitation such as interpolating the FFT sample points around the peak [74, 77]. The frequency offset can be compensated by

$$y_{PN}(t) = y(t) \exp[-j2\pi\Delta \hat{f}t]. \quad (2.17)$$

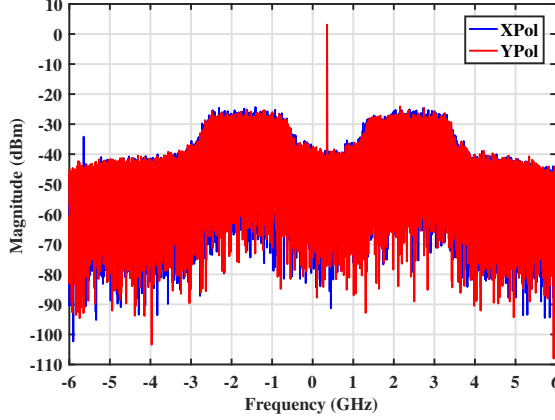


Figure 2.8. Magnitude spectrum of the received signal from experiment with α of 0.67, from Paper A.

Assuming that $\Delta f - \Delta \tilde{f} \approx 0$, (2.17) becomes

$$y_{PN}(t) = x(t) \exp[j\phi(t)] + c \exp[j\phi(t)]. \quad (2.18)$$

The remaining impairment is the phase noise, which as observed in (2.18), can be directly estimated from the second term. Since a frequency guard band was inserted between the pilot tone and the data subcarriers, as shown in Fig. 2.8, in conjunction with the removal of the frequency offset, a low-pass filter (LPF) can be used to extract the pilot tone. The phase of the tone is directly the estimation of the phase noise, $\tilde{\phi}(t)$, and can be represented as

$$\tilde{\phi}(t) = \angle(c \exp[j\phi(t)]). \quad (2.19)$$

Compensation of phase noise can be directly performed by

$$\tilde{y}(t) = y_{PN}(t) \exp(-j\tilde{\phi}(t)), \quad (2.20)$$

where $\tilde{y}(t)$ is the received signal after frequency offset and phase noise compensation. This technique of phase noise estimation and compensation was proposed in [83] and analysed in [84], where it was shown to outperform conventional common-phase error compensation in OFDM. Assuming that $\phi(t) - \tilde{\phi}(t) \approx 0$, then from (2.18)

$$\tilde{y}(t) = x(t) + c, \quad (2.21)$$

where it can be seen that the impairments have been compensated.

This approach presents drawbacks as a result of the insertion of the pilot tone as follows:

1. The required frequency guard band consumes bandwidth.
2. The pilot tone consumes power. If the total transmission power cannot be increased, then the SNR of the data signal at the receiver decreases.
3. High linearity requirement in both the TX and RX to prevent unwanted mixing between the pilot tone and the data signal.

2.4 Practical Considerations

SEFDM must be able to handle practical problems which arise during the transmission. In particular, the issue of timing synchronization carries problematic implications to multicarrier signals without cyclic-prefix. Timing synchronization answers the problem of where the transmission frame begins in burst-mode transmission and also where the start and the end of each SEFDM or OFDM symbols are, since unlike a single carrier system, there is no eye-opening [80]. Incorrect estimation of the symbol timing results in subcarrier dependent phase rotations. This can be seen by considering the timing offset, τ , as delay in the received signal. Ignoring other impairments and AWGN, this is represented as

$$y(t) = x(t - \tau). \quad (2.22)$$

The Fourier transform of (2.22) is

$$Y(f) = X(f) \exp(-j2\pi f\tau). \quad (2.23)$$

Important effect is observed in (2.23). In particular the frequency dependent phase rotation. Since each SEFDM subcarrier is allocated to different frequencies, this implies that under incorrect timing synchronization, the phase of each subcarrier will be rotated differently.

To alleviate this problem, an implementation of the timing synchronization technique developed by Schmedl and Cox for timing synchronization under the presence of frequency offset [80] is used. At the TX-end two OFDM symbols are inserted before the training sequence in one polarization as shown in Fig. 2.5. These two OFDM symbols form timing synchronization (sync) frame. Each of the two OFDM symbols has identical halves (H1 and H2) in time as shown in Fig. 2.9. Each OFDM symbol contains 256 subcarriers carrying 128 pseudo-random QPSK symbols. Notice that the number of symbols is less than the number of subcarriers. This is because one technique to generate identical halves in OFDM symbol is to use only even subcarriers, while the odd subcarriers are null.

At the RX, the received timing synchronization frame, $y_{sync}(t)$, is correlated with a delayed copy of itself. Recalling that the period of OFDM symbol is T seconds, the value of the delay used is $\frac{T}{2}$ seconds. The correlator has two buffers for the signals to be correlated. Each buffer size is $\frac{T}{2}$ seconds worth of signal. The whole process is shown in Fig. 2.10. The peaks of the output of the correlator, $c_{sync}(t)$, correspond to the start positions of both OFDM timing synchronization symbols in the received signal.

The timing synchronization frame also serves an additional purpose. Recalling that the frame is inserted only in one polarization. Therefore, the power ratio between the two polarizations of the received timing synchronization frame can be used for preliminary estimation of the polarization rotation, $\tilde{\theta}$, given by

$$\tilde{\theta} = \arctan\left(\frac{P_Y}{P_X}\right), \quad (2.24)$$

where P_X and P_Y are the received power of the timing synchronization frame in polarizations X and Y, respectively. The compensation can then be performed

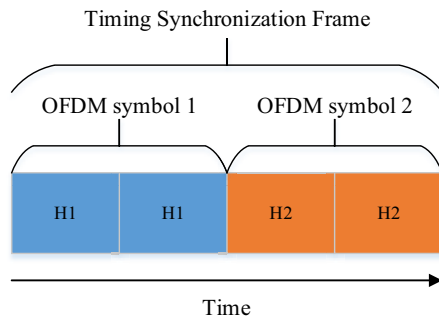


Figure 2.9. Illustration of timing synchronization frame structure.

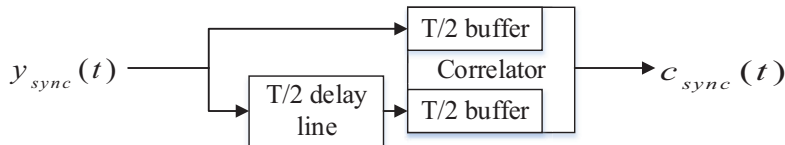


Figure 2.10. Block diagram of timing synchronization.

by [74]

$$\begin{bmatrix} \tilde{\mathbf{R}}_X \\ \tilde{\mathbf{R}}_Y \end{bmatrix} = \begin{bmatrix} \cos \theta & -\sin \theta \\ \sin \theta & \cos \theta \end{bmatrix} \begin{bmatrix} \hat{\mathbf{R}}_X \\ \hat{\mathbf{R}}_Y \end{bmatrix}, \quad (2.25)$$

where $\hat{\mathbf{R}}_X$ and $\hat{\mathbf{R}}_Y$ are the row vectors of the received signal in polarization X and Y, respectively.

Chapter 3

Frequency Multiplier-Based Transmitter

Multiplier-based transmitter (TX) has been proposed as a viable alternative architecture for mm-wave signal generation systems [85]. Previously, research interests in such architecture were focused on low-cost realizations of dual-band TXs utilizing frequency doubler [86–88], e.g., Wireless LAN 2.4 and 5 GHz. Digital predistortion (DPD) of frequency multipliers was proposed by Park *et al.* in 2003 [89], which preceded extensions and improvements in [85, 90–93]. The main challenge with this approach, however, is the trade-off between linearization capability and the complexity of the predistorter. For example, Liu *et al.* demonstrated generations of up to 256-QAM signal at 3.56 GHz using a frequency quadrupler ($\times 4$) linearized by two cascaded stages of DPD [92]. In contrast, this chapter and Paper B present a low-cost low-complexity solution to generate mm-wave signals by utilizing a simple phase retarder predistorter and a frequency multiplier. In addition to simplifying the layout of the whole TX, the multiplier-based architecture is advantageous in relatively low maximum oscillation frequency (f_{max}) technologies, where the multiplier can be used as the power-stage instead of power amplifiers (PAs) [85, 94]. Further, through the exclusion of high frequency LO signals needed in the conventional architecture; the multiplier-based approach has the potential to mitigate the effect of high LO noise floors, which has been proposed to have significant negative impact to the signal quality [10, 11, 95]. These practical benefits create strong incentives for further investigations and research efforts in this area.

3.1 mm-Wave Signal Generation

As recently summarized by Chung *et al.* in [85], the system architectures of high-frequency (mm-wave and sub-THz) TXs can be categorized as follows:

1. A conventional architecture, where an oscillator signal is frequency-multiplied up to mm-wave prior to mixing with the intermediate frequency (IF) or baseband data signals.
2. A multiplier-based architecture, where the IF data signal is frequency-

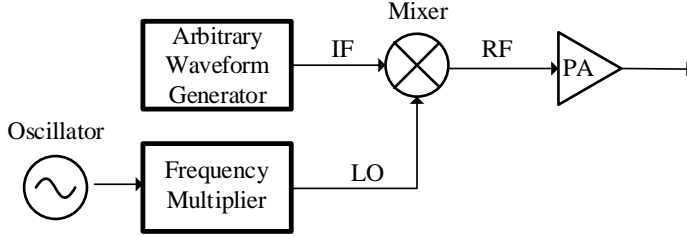


Figure 3.1. A simplified and modified block diagram of the mm-wave TX in [100].

multiplied up to mm-wave.

3. A nonlinear mixer-based architecture, proposed by Takano *et al.* in [96]. The nonlinear mixer mixes the data signal with a low-frequency oscillator signal and upconverts to mm-wave. This architecture has been demonstrated to generate signals up to 300 GHz with frequency tripling ($\times 3$) [94] and doubling ($\times 2$) functionalities [97]. However, this architecture has a severe drawback of unwanted signals being generated at frequencies close to the desired output frequency.

A conventional-architecture mm-wave TX, such as those proposed in [98–100] consists of a high-frequency power-amplifier (PA), high-frequency mixer, one or more frequency multiplier(s), and a relatively low-frequency local oscillator (LO). This common approach avoids the difficulty of realizing high frequency LO and can achieve better frequency stability and phase noise in some technologies [18, 19]. Alternatively, instead of the frequency multiplier(s) and low-frequency LO pair, a high-frequency mm-wave LO may be realized such as that in [101]. Finally, a middle-ground combination of the two approaches has also been proposed [102].

The block diagram of the mm-wave TX in [100] is modified for simplification and shown in Fig. 3.1. For practicality of the discussions, baseband signal generation is represented by an arbitrary waveform generator (AWG). The AWG is assumed to generate intermediate frequency (IF) data signals to the mixer. A low frequency oscillator is injected into a frequency multiplier which outputs an oscillator signal at the desired mm-wave frequency to the mixer. The output of the mixer is ideally upconverted IF signals, which are subsequently amplified by the PA to suitable transmission power levels. In summary, this conventional architecture contains five main components: AWG, oscillator, frequency multiplier, mixer, and PA.

3.2 Multiplier-Based Transmitters

For multiplier-based TX architecture, a frequency multiplier is used to directly upconvert the IF signal. For illustration, see Fig. 3.2. Direct comparisons can



Figure 3.2. A simplified block diagram of an upconverting TX using frequency multiplier.

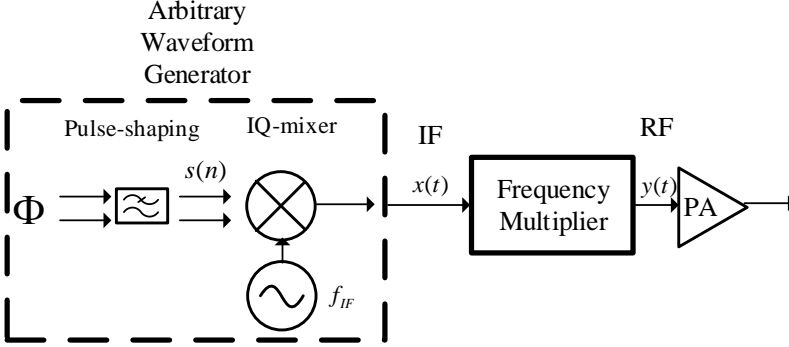


Figure 3.3. A simplified block diagram of an upconverting TX using frequency multiplier with AWG functionality shown.

be made to the conventional TX in Fig. 3.1; it can be seen that the IF output of the AWG is directly injected to the frequency multiplier, which outputs the radio frequency (RF) mm-wave signal to the PA for further transmission. This technique has three main components: AWG, frequency multiplier, and PA. This architecture can be sub-categorized into two variants: with DPD [85–88, 90, 92, 93] and without [103]. To the author’s best knowledge, reported experimental demonstrations of multiplier-based TX at mm-wave consist of [85] at 63 GHz and [103] at 240 GHz, both used frequency triplers ($\times 3$), and in Paper B at 78.6 GHz using a frequency sextupler ($\times 6$). Other reported demonstrations are at frequencies below 30 GHz, especially 2.4 and 5 GHz Wireless LAN dual-band TXs [86, 87], which can be considered as hybrids between conventional TX and multiplier-based TX. These hybrid systems are based on conventional TXs, but the bias points of the PA can be adjusted such that it acts as a frequency multiplier, effectively supporting dual-band transmission [86–88].

3.2.1 Frequency Multiplier Nonlinear Model

For clarity and for later use, Fig. 3.2 is now expanded to illustrate the functions of the AWG in the context of this work, as shown in Fig. 3.3. The complex

data symbols, Φ , are pulse-shaped to generate the complex baseband signal, $s(n)$, which may be represented as

$$s(n) = |s(n)| \exp(j\phi_s(n)), \quad (3.1)$$

where j is $\sqrt{-1}$ and $\phi_s(n)$ is the phase of the signal. After digital to analog conversion to $s(t)$ and upconversion to IF at f_{IF} Hz.

$$x(t) = \text{Re}\{s(t) \exp(j(2\pi f_{IF}t + \phi_{PN}(t)))\}, \quad (3.2)$$

where $\phi_{PN}(t)$ is the phase noise. Equation (3.2) can be expanded to

$$x(t) = |s(t)| \cos(2\pi f_{IF}t + \phi_s(t) + \phi_{PN}(t)). \quad (3.3)$$

Using memoryless polynomial model to represent the frequency multiplier and assuming ideal harmonics termination; the RF output, $y(t)$, of a frequency multiplier with frequency multiplication factor, β , when fed with $x(t)$ may be described as

$$y(t) = \sum_{k=1}^K r_k |s(t)|^{\beta+2(k-1)} \cos(2\pi(\beta f_{IF})t + \beta\phi_s(t) + \beta\phi_{PN}(t)), \quad (3.4)$$

where K is the nonlinear order, and r_k is the real-valued nonlinear coefficients. Note that some reports argue that the modelling accuracy of some frequency multipliers can be improved if memory terms are included [91].

3.2.2 Output Impairments

Observing (3.4), it can be seen that the RF is at βf_{IF} Hz as intended. However, the signal is severely impaired by the following:

1. The distortion of the phase of the data signal, $\beta\phi_s(t)$.
2. The worsened phase noise, $\beta\phi_{PN}(t)$. This impairment is not exclusive to the upconverting TX using frequency multiplier technique. A conventional-architecture TX that uses frequency multiplier to upconvert an oscillator signal is also affected.
3. The amplitude nonlinearity, $|s(t)|^{\beta+2(k-1)}$.

These impairments contribute to the distortion of the transmitting signal, e.g., the bandwidth expansion effect, where the bandwidth of the RF signal expands relative to the IF signal by a function of β .

3.2.3 Existing Approaches

To address the impairments, DPD can be used to predistort the input IF signal. However, due to the strong nonlinearity of a frequency multiplier, the required DPD is typically complex. Another approach is to entirely exclude DPD and rely instead on the fixed relationship between the frequency multiplication factor, β , and the constrained phases of the complex symbols, e.g., the four phases of QPSK symbols, or the eight phases of 8-PSK symbols. For example,

consider transmitting QPSK signals through a frequency tripler ($\beta = 3$). Due to the relationship between the phases of QPSK symbols and β , the equivalent transmitting symbol points merely switches their phases. To illustrate, let Φ_{QPSK} represent QPSK symbols:

$$\Phi_{QPSK} = \exp(j(2\eta - 1)\frac{\pi}{4}) \quad (3.5)$$

such that $\eta \in \{1, 2, 3, 4\}$. Assuming ideal rectangular pulse-shaping and upconversion to IF, the resulting signal is fed to a frequency tripler; the RF output from (3.4) then becomes

$$y(t) = \sum_{k=1}^K r_k \cos(2\pi(3f_{IF})t + 3(2\eta - 1)\frac{\pi}{4} + 3\phi_{PN}(t)). \quad (3.6)$$

Interestingly, the phase distortion is reduced to $3(2\eta - 1)\frac{\pi}{4}$ which means that the phases of the original symbols distinctively translate to those of other symbols, while retaining the original constellations of QPSK, i.e., $\frac{\pi}{4}$ to $\frac{3\pi}{4}$ rad, $\frac{3\pi}{4}$ to $\frac{\pi}{4}$ rad, $\frac{5\pi}{4}$ to $\frac{7\pi}{4}$ rad, and $\frac{7\pi}{4}$ to $\frac{5\pi}{4}$ rad. This means that different symbols retain their distinctions and can be decoded at the receiver (RX). However, an ideal rectangular pulse-shape cannot be generated in practice and the transition between different symbols do not adhere to the aforementioned relationship between the symbol phases and β , which is required for the generation without the phase distortion. This practicality results in nonlinear distortion and most particularly the bandwidth expansion effect. Furthermore, the distorted transition regions affect the processing requirements at the RX; even though the equivalent symbol points retain the phases of QPSK symbols, the DSP algorithms at the RX, e.g., symbol synchronization, must be able to handle the severe distortion of the transition regions.

3.3 Upconverting Transmitter Using Frequency Multiplier Coupled with Phase Retarder

The work in this thesis proposes the use of a phase retarder, a component which “slows” the revolution of the phase of the IF signal. This technique is a compromise between the two existing approaches, namely, the high computational complexity of a full-fledged DPD and the transmission with full distortion. The technique is suitable for transmission of constant-modulus modulations, e.g., QPSK, 8-PSK, 16-PSK. Paper B has experimentally demonstrated the technique at mm-wave RF of 78.6 GHz using frequency sextupler ($\beta = 6$) to transmit 8-PSK signals at up to 4.8 Gbit/s.

3.3.1 Phase Retarder

The complex baseband signal, $s(n)$ in (3.1), is predistorted using a phase retarder before upconversion to IF as shown in Fig. 3.4. The operation of the phase retarder is described as

$$\phi_{PR}(n) = \frac{\phi_s(n) + 2\pi c(n)}{\beta}, \quad (3.7)$$

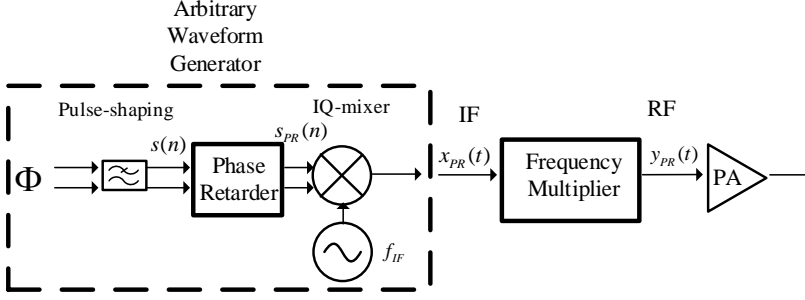


Figure 3.4. A simplified block diagram of an upconverting TX using frequency multiplier and phase retarder.

where $c(n)$ is an arbitrary integer to represent phase unwrapping operation whose value may change with different sample index, n . The phase retarder operates only on the phase of the input signal. The unwrapped phase is divided by β . The phase retarder therefore “retards” the development of the phase over time. The name is inspired by a braking instrument commonly found in heavy vehicles. The retarded phase, ϕ_{PR} , then supersedes the original phase of $s(n)$, giving

$$s_{PR}(n) = |s(n)| \exp(j\phi_{PR}(n)), \quad (3.8)$$

which is then upconverted to IF.

3.3.2 Compensated Nonlinearity

With (3.8) as the new baseband signal, the IF signal from (3.3) becomes

$$x_{PR}(t) = |s(t)| \cos(2\pi f_{IF}t + \phi_{PR}(t) + \phi_{PN}(t)). \quad (3.9)$$

After injecting the phase retarded IF signal in (3.9) to the input of the frequency multiplier. The RF output from (3.4) then becomes

$$y_{PR}(t) = \sum_{k=1}^K r_k |s(t)|^{\beta+2(k-1)} \cos(2\pi(\beta f_{IF})t + \phi_s(t) + \beta\phi_{PN}(t)), \quad (3.10)$$

where it can be observed that the distortion of the phase of the data signal in (3.4) has been resolved, since $\phi_s(n) = \phi_s(n) + 2\pi c(n)$ rad. Furthermore, it has been experimentally shown in Paper B that the unwanted effect of bandwidth expansion is also suppressed. An experimental result is presented in Fig. 3.5, which shows the received power spectral densities (PSD) with and without the phase retarder. Full description of the experiment is found in Paper B. However, it can also be observed in (3.10) that the amplitude nonlinearity remains unaddressed at the TX, resulting in compatibility limitations with multi-modulus symbols, e.g., 64-QAM, 256-QAM. This issue along with the worsened phase noise are addressed at the digital RX.

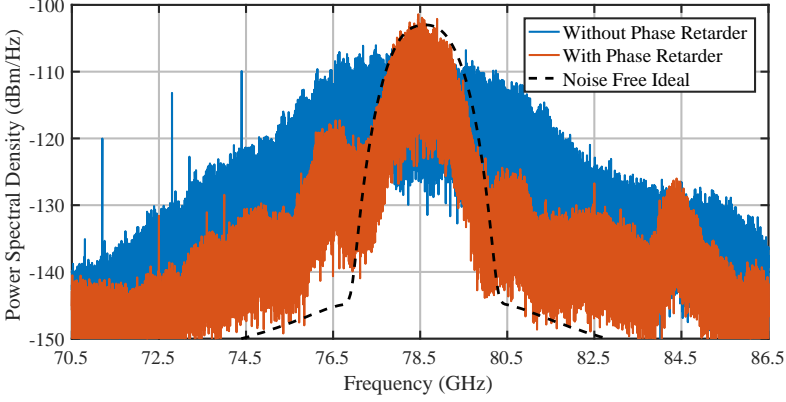


Figure 3.5. PSDs of the received signal with and without phase retarder. Noise-free ideal PSD is provided as reference. Data taken from the experiment in Paper B.

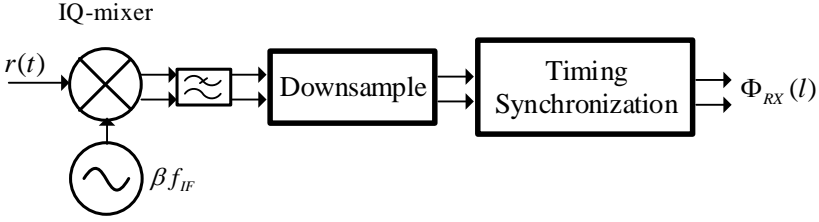


Figure 3.6. A simplified block diagram of the preliminary (front-end) stage of the digital RX.

3.4 Digital Receiver

A purpose-built digital RX was developed to mitigate the remaining amplitude nonlinearity and worsened phase noise in the transmitted signal. At the RX, the received signal, $r(t)$, is downconverted to complex baseband, low-pass filtered, downsampled to symbols, and timing synchronized. This front-end process, shown in Fig. 3.6, outputs the received complex symbols, $\Phi_{RX}(l)$, where l is the symbol-index.

3.4.1 Post-Distorter

To compensate the remaining amplitude nonlinearity, a memory polynomial model [104] was used for post distortion. The order of the model depends on β such that if β is odd, the model is odd-ordered and if β is even, the model is even-ordered. The coefficients are estimated by assigning some transmitting

symbols as pilots, $p_{TX}(l)$. The process is described as

$$p_{TX}(l) = \sum_{m=0}^M \sum_{k=0}^K c_{m,k} p_{RX}(l-m) |p_{RX}(l-m)|^{2k+\beta-1}, \quad (3.11)$$

where $c_{m,k}$ is the complex coefficients to be estimated. M is the memory depth to handle the memory effect, if any. $p_{RX}(n)$ are the received pilot symbols. After estimation of the coefficients, the received symbols can then be post-distorted through

$$\tilde{\Phi}_{RX}(l) = \sum_{m=0}^M \sum_{k=0}^K c_{m,k} \Phi_{RX}(l-m) |\Phi_{RX}(l-m)|^{2k+\beta-1}, \quad (3.12)$$

where $\tilde{\Phi}_{RX}(l)$ is the post-distorted symbol.

3.4.2 Phase Error Compensator

This subsection refers to phase noise and any impairment of the phase of the received symbols as “phase error”. The post-distorted symbols are stripped of modulation using Viterbi-Viterbi algorithm [76]. A comparison of the PSD estimates before and after Viterbi-Viterbi obtained from the experiment described in Paper B is given in Fig. 3.7. It can be seen that the spectrum of the transmitted symbol sequence has been transformed into a single tone carrying phase error information. The phase of the resulting complex tone is then measured, unwrapped, and scaled as a function of time. The phase development is then low-pass filtered to obtain an estimation of the phase error as a function of time, which is subsequently used for compensation. Without low-pass filtering the compensation is equivalent to standard hard detection of the symbols [105].

The probability density function (PDF) of the phase error with and without the above phase error compensation as observed in the experiment described in Paper B is shown in Fig. 3.8, where improvements can be seen.

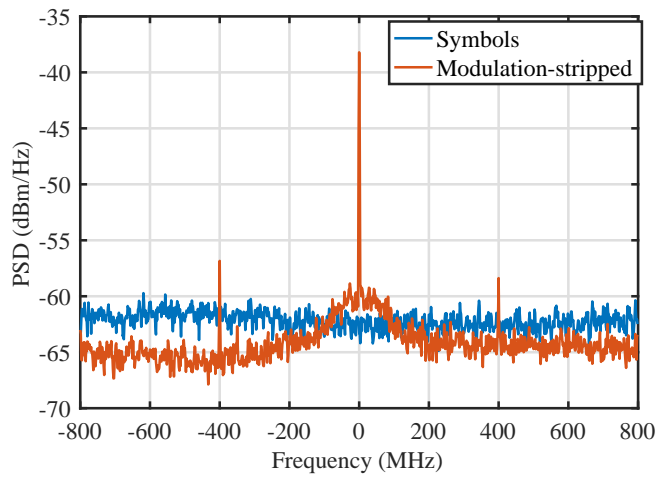


Figure 3.7. Experimentally obtained PSD estimates before and after Viterbi-Viterbi algorithm, before is denoted as “Symbols” and after as “Modulation-stripped”.

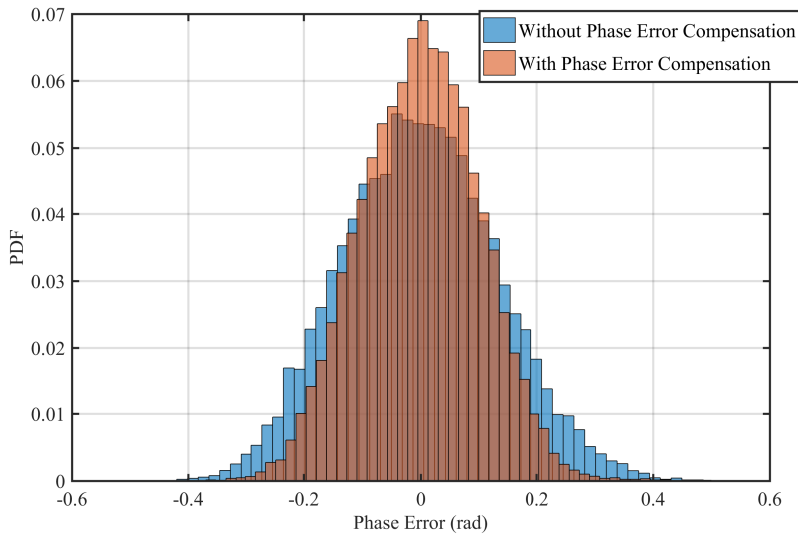


Figure 3.8. PDF of the phase error with and without phase error compensation obtained from the experiment described in Paper B.

Chapter 4

Emulation of Mutual Coupling for Characterization and Evaluation Measurements

Millimeter wave (mm-wave) and Massive Multiple-Input Multiple-Output (MIMO) are recognized as two of the most disruptive technologies in the development of next generation wireless systems [106]. Massive MIMO promises improved spectral efficiency, spatial diversity in channel response, and simple transmit and receive structures [107]. It achieves these characteristics through the utilization of large antenna arrays, i.e., large number of antennas, power amplifiers, and transmission paths, which can be in the order of several hundreds. Such architecture has been shown to provide higher transmission capacity [108]. However, one of the main challenges in the utilization of such large arrays is the interactions between the array elements. Such interactions can include signal, thermal, and mechanical couplings. In the scope of this thesis and Paper C, we focus on the well-known issue of signal or mutual coupling [20], which results in undesirable effects including cross-talks and variations of load reflection coefficients at various points in the systems (load-pull effects) [109]. These impairments negatively affect the system KPIs by reducing power and spectral efficiencies and distorting the transmitted signals [110].

Output signal or mutual coupling happens when the output of a transmission path “leaks” or gets coupled to the other transmission paths. This in turn varies the output impedance of the corresponding power amplifiers (PA). Such phenomenon can be mitigated by using isolators to prevent the coupled signal from reaching the PA [111]. However, employing isolators in a large antenna array not only reduces the level of integration, but is simply an expensive manoeuvre. This motivates the efforts to study and understand the coupling effects especially with respect to the transmitting signal distortion, and the penalty incurred to the system KPIs.

Research efforts addressing Massive MIMO are in abundant. Several Massive MIMO experimental test beds have been developed by both the industry [112]

and the academy [113–116]. Various behavioral modelling approaches have been proposed to represent [117, 118] and predistort [119] antenna coupling effects in such systems. In contrast to these, we design and build measurement technique and system to emulate coupling without requiring the large array and several hundreds of elements to be realized. Devices and components can then be evaluated under such conditions and the penalty incurred upon the system KPIs measured. The technique was first proposed in Paper CP1, improved in Paper CP3, and subsequently finalized in Paper C.

4.1 Brief Overview

The proposed technique has minimal experimental setup requirement; only one PA has to be realized if identical elements are used in the array. To represent each transmission path, a time-division multiplexing scheme is developed. In each time-slot, the PA acting as the device under test (DUT) is presented with the time-varying load reflection coefficients of the corresponding transmission path. The coefficients are determined by the predefined S-parameter coupling network. The technique is based on wide-band active loadpull [21], but unlike standard loadpull, the technique converges to the S-parameter coupling network instead of load reflection coefficients.

The distorted signal under the emulated coupling effects can then be evaluated in terms of the penalty to the KPIs which may be measured through: adjacent channel power ratio (ACPR), error-vector magnitude (EVM), normalized mean-square error (NMSE), and bit-error rate (BER). The emulation method is versatile and can be applied to emulate specific scenarios. For example, beamforming and Massive MIMO arrays have different characteristics of the transmission paths and signals, which in turn change the coupling effects.

4.2 Antenna Array Applications for Communication

Usage of antenna arrays in communication systems has been investigated since the first half of the 20th century as shown through the work in [120–123]. The aspiration for this development is due to the desire for a directive radiation system. As stated in [120], the first proposal of such array is by Brown in 1899 as evidenced by his patent [124], which was subsequently followed by improvements and modifications [125, 126].

In modern days, antenna arrays have integral incumbent roles in communication systems, as can be seen through the surge in the popularity of very large array-enabled system such as Massive MIMO [107, 127]. As summarized by Paulraj *et al.* [128], a modern MIMO system provides performance improvement which may be categorized as follows:

1. Array gain, to increase the average received SNR.
2. Diversity gain, in particular, spatial diversity to mitigate fading channels.
3. Spatial multiplexing gain, to offer improvement in capacity which scales linearly to the minimum number of TX and RX antennas.

4. Interference reduction, to avoid interference to adjacent units.

Massive MIMO enhances these benefits through the large number of antennas. As a result, it has the potential to increase the transmission capacity through aggressive spatial multiplexing, while simultaneously improving the energy efficiency [127].

Due to the aforementioned benefits offered by Massive MIMO, there is a strong incentive to investigate the implementation of such system at mm-wave frequencies; supported by the smaller spacing between elements in the array. As a consequence, the deployment of bulky and costly isolators to suppress mutual coupling is impractical.

4.3 Antenna Array Output Coupling

This section describes the generic working model of mutual coupling to facilitate the description of the measurement technique. An arbitrary antenna array is shown in Fig. 4.1, which includes:

1. N transmission paths, where N is a positive integer
2. N TXs
3. N PAs
4. N load reflection coefficients, Γ_{load}
5. S-parameter network, an $N \times N$ matrix \mathbf{S} , connected to the output of all transmission paths. The network defines the magnitude and phase (or rather delay) of coupling between each pairing of transmission paths.
6. The incident and reflected waves (a_1, b_1, a_2 , and b_2) defined at the input and output ports of each PA. Notation is as indicated in the figure, i.e., $a_2^{(i)}$ is the incident wave on the output of the i^{th} PA.

The S-parameter network can be defined as

$$\mathbf{S} = [S_{ij}]_{i,j \in 1,2,\dots,N} = \begin{bmatrix} S_{11} & S_{12} & \cdots & S_{1N} \\ S_{21} & S_{22} & \cdots & S_{2N} \\ \vdots & \vdots & \ddots & \vdots \\ S_{N1} & S_{N2} & \cdots & S_{NN} \end{bmatrix}, \quad (4.1)$$

where S_{ij} is the signal coupling from the j^{th} to the i^{th} transmission path. The load reflection coefficients of the i^{th} transmission path, $\Gamma_{load}^{(i)}$, is

$$\Gamma_{load}^{(i)} = \frac{a_2^{(i)}}{b_2^{(i)}}. \quad (4.2)$$

Given a well-matched array ($S_{ii} = 0$), the a_2 wave of the i^{th} PA is

$$a_2^{(i)} = \sum_{\substack{j=0 \\ j \neq i}}^N S_{ij} b_2^{(j)}. \quad (4.3)$$

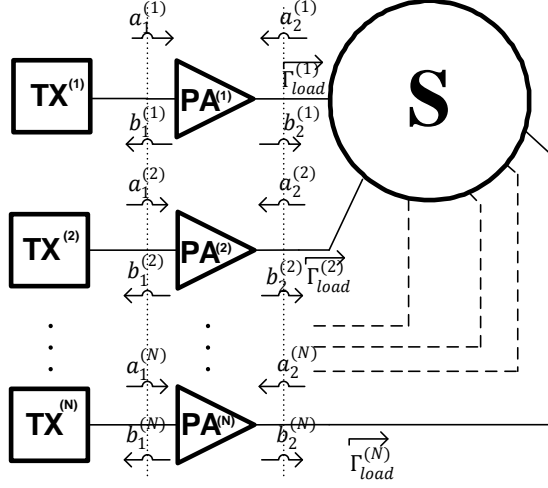


Figure 4.1. Generic antenna array with N transmission paths, from Paper C.

Note that the notation $\cdot^{(i)}$ in $a_2^{(i)}$, $\Gamma_{load}^{(i)}$, and other following terms in this chapter indicates the index of the transmission path. Using (4.3) in (4.2) gives

$$\Gamma_{load}^{(i)} = \frac{\sum_{j=1}^N S_{ij} b_2^{(j)}}{b_2^{(i)}} - S_{ii}. \quad (4.4)$$

The emulation technique developed in this thesis presents a method to generate the time-varying load reflection coefficients in (4.4). Observation of (4.4) reveals that, if the coupling network is known, this goal can be achieved through realizations of all b_2 waves.

4.4 Emulation Method

This section describes the emulation process of mutual coupling in an antenna array.

4.4.1 Overview

The realization of each b_2 wave is both the goal and the means of the emulation procedure, i.e., the b_2 wave of a transmission path is simultaneously influenced by and influencing those of other transmission paths; such characteristic can be represented by an iterative process. Observing (4.3), it can be seen that the incident wave, a_2 , of each transmission path is a function of coupling (defined by \mathbf{S}) and the reflected waves, b_2 , of other paths. The input waveform to each PA, a_1 , on the other hand, is the signal intended for transmission of the

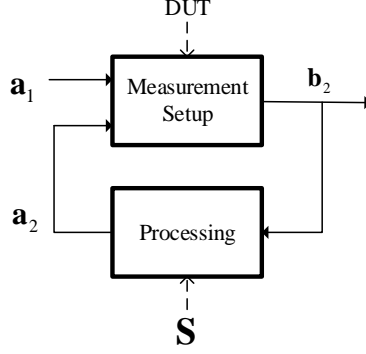


Figure 4.2. Simplified block diagram representing the emulation procedure.

corresponding transmission path and is assumed not to be affected by the mutual coupling. Furthermore, to realize a minimal low-cost low-complexity measurement setup, a constraint of using only one PA as the DUT is added to the consideration. These observations and constraint can be arranged and simplified into a block diagram shown in Fig. 4.2, where \mathbf{a}_1 , \mathbf{a}_2 , and \mathbf{b}_2 are time-domain vectors of a_1 , a_2 , and b_2 of all transmission paths, respectively. In the figure, the measurement setup block operates on the characteristics of the DUT through active load-pulling. The processing block operates on the S-parameter coupling network and computes \mathbf{a}_2 according to (4.3).

4.4.2 Offline Processing Unit

Constraints: the coupling effects of all N transmission paths have to be emulated under the constraint of having one DUT.

Solutions: Utilize time-division multiplexing where there are multiple time-slots. In each time-slot, only one transmission path is emulated, as shown in Fig. 4.3. The figure illustrates the operations to emulate the i^{th} transmission path in the i^{th} time-slot. To emphasize on the time-division aspect, the “processing” block in Fig. 4.2 is now noted as “offline processing unit”, which contains a buffer, a filter array, and a combiner. The emulated reflected waves of other transmission paths, $b_2^{(j, j \neq i)}$, which were buffered from previous time-slots, are passed through an array of filter. These filters amplitude-scale and time-shift the signals to the corresponding coupling levels as determined by the S-parameter network. The filtered signals are then superimposed into the coupled signal of the i^{th} transmission path, $a_2^{(i)}$, which is sent to the measurement setup along with the transmitting signal, $a_1^{(i)}$. The measurement setup then operates on the DUT and outputs the distorted signal of the i^{th} transmission path, $b_2^{(i)}$, which is sent to the buffer, to be used in other time-slots.

The emulation of N time-slots is not sufficient to complete the emulation, because the process for the first transmission path does not have prior information on other transmission paths in the buffer. Hence, the iterative nature of

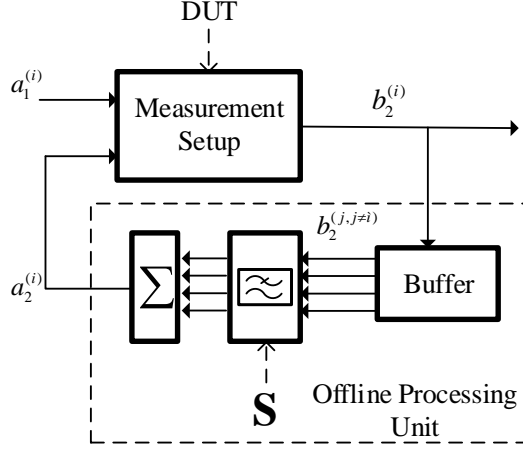


Figure 4.3. Simplified block diagram representing the emulation of the i^{th} transmission path in the i^{th} time-slot.

the technique, where N time-slots form an iteration. The number of iterations required is dependent on the particular transmission scenario of interest. The emulation is deemed complete only after the output of all transmission paths converge. After the final iteration, N time-varying stable solutions are obtained from the emulation. In practice, the convergence goal can be implemented through monitoring of the normalized mean-square error (NMSE) between $b_2^{(i)}$ from an iteration with the previous iteration, as an example. Table I in Paper C illustrates this iterative procedure in detail.

4.4.3 Measurement Setup

The block “measurement setup” in Fig. 4.3 is expanded and shown in Fig. 4.4. The measurement setup consists of the following:

1. a PA as the DUT
2. a driving amplifier (*driver*)
3. an isolator to prevent reflection to the output of the *driver*
4. a directional coupler
5. two TXs (TX1 and TX2)
6. two RXs (RX1 and RX2)

The DUT and TX1 form “transmission path under test” (TPUT), which represents the intended transmitting signal of the i^{th} transmission path, $a_1^{(i)}$. The *driver* and TX2 form “coupling path under test” (CPUT), which represents

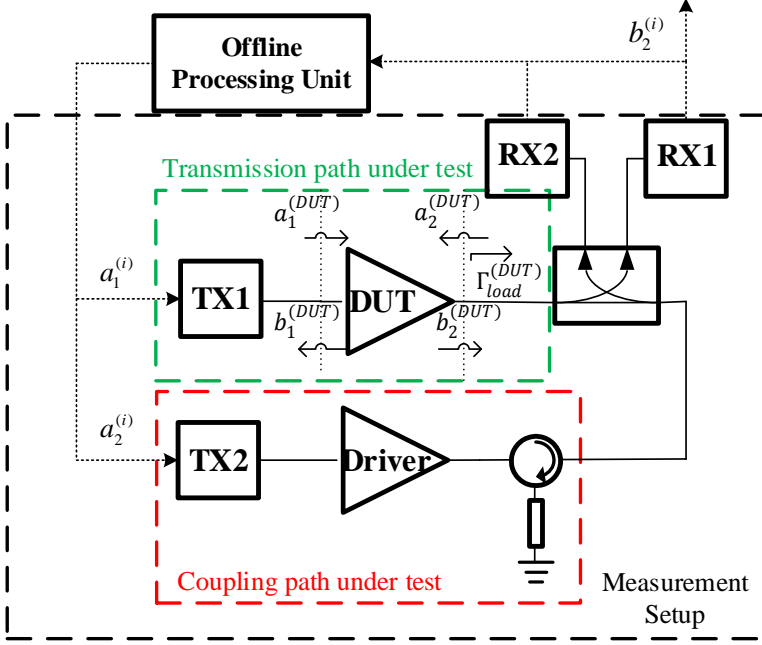


Figure 4.4. Complete block diagram describing the emulation of the i^{th} transmission path in the i^{th} time-slot, modified from Paper C.

the output coupling signal of the i^{th} transmission path, $a_2^{(i)}$. The *driver* merely serves to increase the coupling power to sufficient levels and must be operated in its linear region. RX1 receives the distorted transmitting signal, $b_2^{(i)}$, which is sent to the offline processing unit as described. To illustrate, a simple example of this procedure for a two-element array with identical signals is provided in Section III-C of Paper C.

4.4.4 Isolation of Coupling Effects

The emulated transmitting waveforms are not only distorted due to the coupling effects, but also the distortion of the PA under standard 50- Ω termination. This may not be the desirable outcome depending on the specific scenario the user is aiming to emulate. Most importantly, in certain scenarios, the 50- Ω termination nonlinearity may prevent meaningful emulation of lower coupling levels, since in such cases, the distortion of the waveforms is dominated by the 50- Ω termination nonlinearity. To enhance the coupling levels that can be emulated (coupling dynamic range), the transmitting signal of each transmission path is predistorted using digital pre-distortion (DPD). The predistorted signal, $\tilde{a}_1^{(i)}$, is then sent to the measurement setup as illustrated in Fig. 4.5.

In order to linearize the DUT when terminated with 50- Ω , an odd-order memory polynomial model was used [129–131]. Denoting the complex baseband input signal to the model as, $x(n)$, the output signal, $y(n)$, can be represented

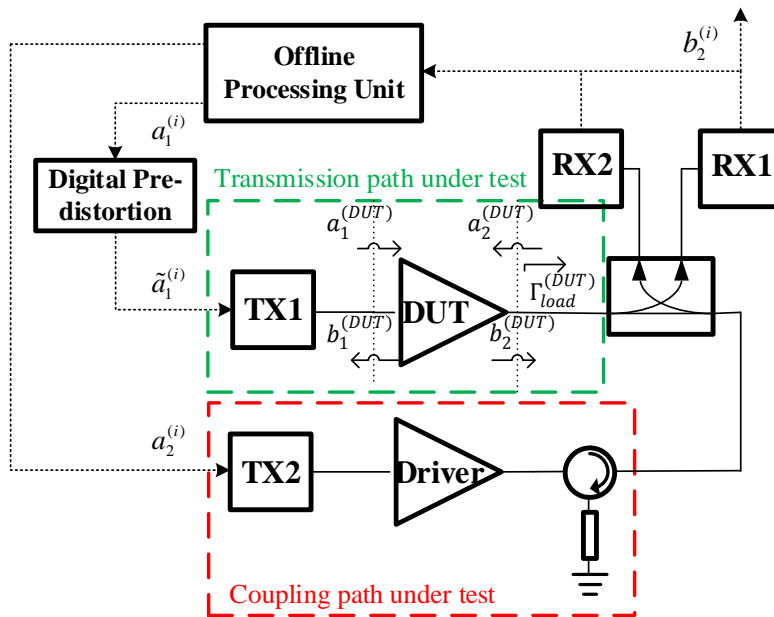


Figure 4.5. Complete block diagram of the emulation technique with digital pre-distortion in the i^{th} time-slot, emulating the i^{th} transmission path, modified from Paper C.

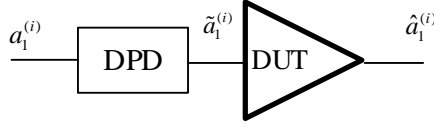


Figure 4.6. Digital pre-distortion goal.

as

$$y(n) = \sum_{k=0}^{\frac{K-1}{2}} \sum_{m=0}^M b_{k,m} x(n-m) |x(n-m)|^{2k}, \quad (4.5)$$

where K is the maximum order, M is the memory depth, and $b_{k,m}$ are the linearization parameters to be estimated. To utilize this model as DPD, the estimation goal is set such that $a_1^{(i)}$ is $x(n)$, and $\tilde{a}_1^{(i)}$ is $y(n)$, which is connected to the input of the DUT as shown in Fig. 4.6. The output of the DUT is denoted as $\hat{a}_1^{(i)}$, which is desired to be the same as $a_1^{(i)}$ when terminated with 50Ω .

In this thesis, the estimation of linearization parameters is done using a variant of Indirect Learning Architecture [132], proposed in [133]. The advantage of this variant is in the removal of the needs for DUT gain normalization in the estimation iterative loop. In practice, the linearization parameters are not estimated per transmission path as might have been suggested in Fig. 4.6. Rather, an arbitrary wideband modulated test signal was used to obtain the parameters, which are subsequently applied to all transmission paths.

The importance of this step is illustrated in Fig. 4.7, which shows a comparison of the DUT output signal power spectral densities (PSDs) with and without DPD. The PSD without DPD exhibits spectral regrowth, which is suppressed, to a certain extent, when DPD is implemented.

Finally, Fig. 4.8 shows the results which are experimentally obtained from the emulation of the aforementioned two-element array example scenario, described in Section III-C of Paper C. The emulated transmitting waveforms at coupling level ($-20 \log(|S_{ij}|)$) from 8.5 to 38.5 dB are evaluated in terms of the KPIs: adjacent channel power ratio (ACPR) representing out-of-band distortion, NMSE quantifying overall distortion, and error-vector magnitude (EVM) which is indicating the in-band distortion. Observing the ACPR, the results obtained without DPD spans from -35.1 dBc at lower coupling level to -33.5 dBc at higher coupling level, giving a span of 1.6 dB. On the other hand, the ACPR obtained with DPD exhibit a much wider span of 3.7 dB. The same trend is observed in NMSE which has a span of 1.96 dB without DPD and 3.63 dB with DPD. Contradictory and interestingly, the in-band distortion quantified through EVM shows spans of 0.810% without DPD and 0.546% with DPD. This is because the EVM became stable when coupling level decreases down to -20 dB, which indicates SNR-limited results.

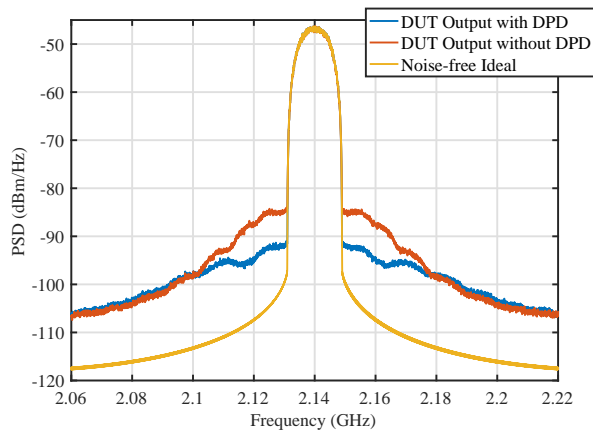
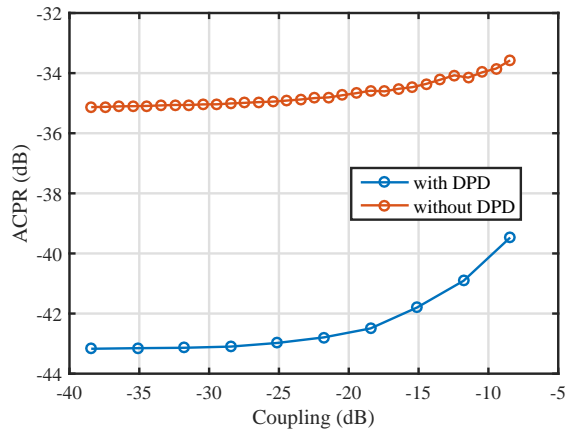
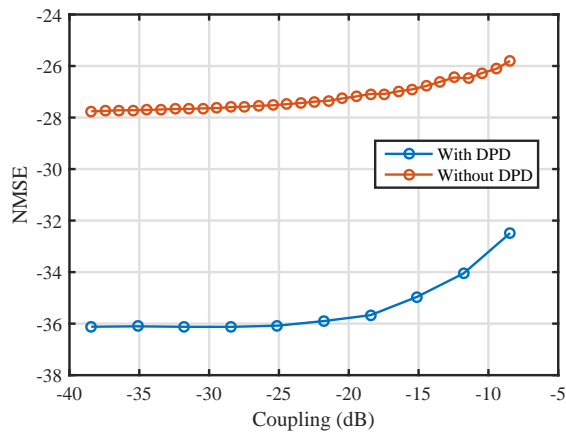


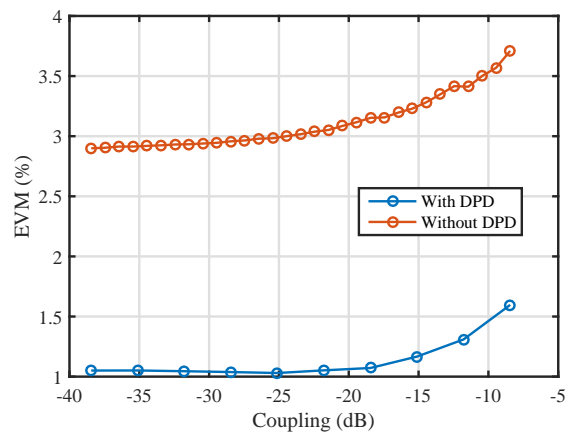
Figure 4.7. Comparison of the DUT output signal PSDs with and without digital pre-distortion, noise-free ideal signal is included as reference, from Paper C.



(a)



(b)



(c)

Figure 4.8. Comparisons of emulated signals at varying coupling level with and without DPD through: (a) ACPR from Paper C, (b) NMSE, and (c) EVM.

4.4.5 Calibration

To ensure and preserve both the coupling power levels and phases prescribed by the coupling S-parameter network, \mathbf{S} , calibration must be performed to shift the reference planes of the measurement setup to the input and output of the DUT, marked by the two dash lines in Fig. 4.4 and 4.5. During the emulation of the i^{th} transmission path, the TPUT input waveform, $a_1^{(i)}$, must be projected onto $a_1^{(DUT)}$, while simultaneously the CPUT input waveform, $a_2^{(i)}$, must be projected onto $a_2^{(DUT)}$ such that the coupling defined by \mathbf{S} is true and maintained. To achieve this, a standard reciprocal-short-open-load procedure described in [134] was performed. Furthermore, a power meter was used to obtain the absolute output power levels of the TXs [135]. An additional step of phase calibration was also performed to eliminate any parasitic anomalies [136].

4.5 Applications

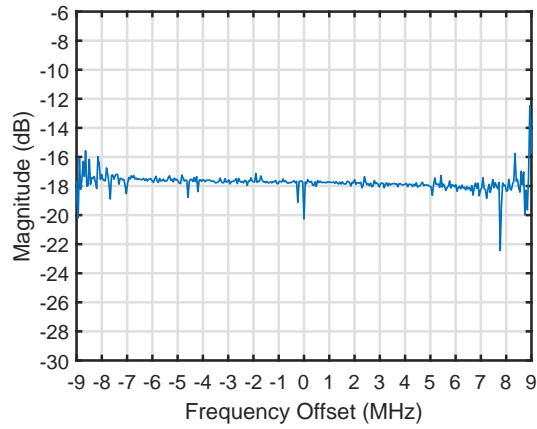
The emulation technique provides flexibility in both the measurement setup and the processing blocks in Fig. 4.2. Depending on the scenario to be emulated, e.g., an array with different PAs, more DUTs may be added to the measurement setup block. Furthermore, the array maybe designed for a specific purpose such as beamforming or Massive MIMO, which have different characteristics of the transmitting signals. This characteristic may be quantified through the cross-correlations of the signals in different transmission paths.

In beamforming scenario, identical signals are transmitted in different transmission paths. The delay between each path defines the steering angle [137]. Without phase differences, e.g., steering broadside in a broadside array, the cross-correlation coefficients are unity indicating identical signals, resulting in a certain coupling effect. Upon applying phase shift or time-delay, the steering angle varies and the cross-correlation coefficients decrease, and thus the coupling effect changes. To illustrate, Fig. 4.9 shows the load reflection coefficients in beamforming scenario with and without delay between transmission paths.

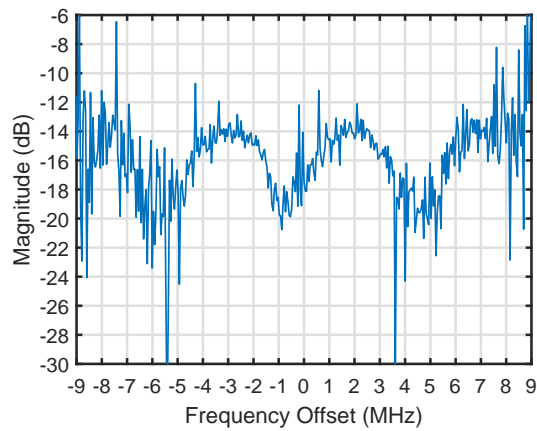
In Massive MIMO for spatial multiplexing gain, the signals in each transmission paths are independent giving cross-correlation coefficients approaching zero. This results in characteristics of the coupling effect, which are less dependent on the delay between transmission paths as illustrated in Fig. 4.10.

The emulation technique is fully suitable to emulate and take into consideration these different scenarios and their implications on the coupling effects to fully represent the array of interest. This has been thoroughly demonstrated and verified in Paper C.

With minimal setup requirements in both the number of components and computation complexity, the technique is suitable for rapid evaluations and characterizations of components under mutual coupling effects without the need to realize an actual array. Ultimately, the technique is an appealing and valuable tool for circuit and system designers to foresee how the DUT would perform in real usage scenarios and to be able to characterize and evaluate their designs with system-level KPIs.

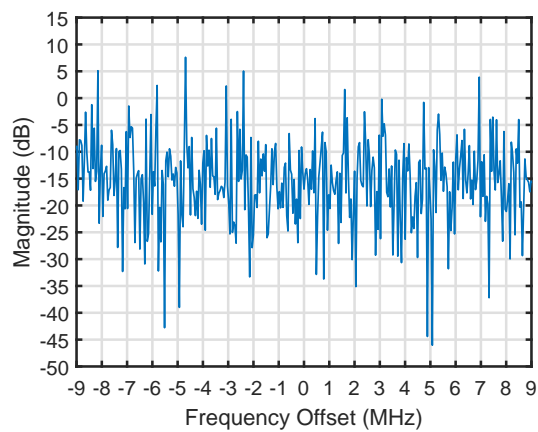


(a)

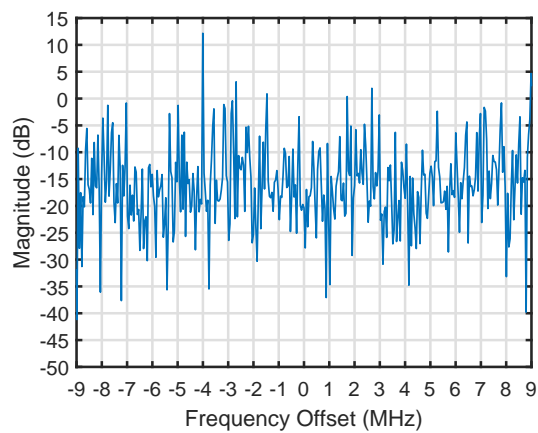


(b)

Figure 4.9. Magnitude of emulated load reflection coefficients in a beamforming scenario with coupling level of 16.46 dB and delay between transmission paths of (a) null and (b) two symbol periods, from Paper C.



(a)



(b)

Figure 4.10. Magnitude of emulated load reflection coefficients in a Massive MIMO scenario with coupling level of 16.46 dB and delay between transmission paths of (a) null and (b) one symbol period, from Paper C.

Chapter 5

A Technique to Measure Reflection and Transmission Coefficients

With the advent of devices, circuits, sub-systems, and systems which support mm-wave frequencies and mobilize wider bandwidths; common practice measurements at lower frequencies need to be re-investigated in order to enhance their usability and practicality under the new regime.

This chapter will investigate a technique to measure reflection and transmission coefficients with the following goals: to improve the precision of existing measurement instruments and to construct a tool enabling new characterizations. The approach undertaken is to mobilize DSP practices in conjunction with those of instrumentation.

Note that this chapter and Paper E use the following definitions:

- Accuracy refers to the statistical bias and systematic error.
- Precision refers to the statistical variability and stochastic error.

These are in contrast to the definitions used by the International Organization for Standardization, where accuracy is both systematic and stochastic errors.

5.1 Applications of Transmission and Reflection Coefficients

Chapter 4 has introduced a technique to emulate antenna array mutual coupling effects, which are prescribed by the S-parameter matrix, \mathbf{S} , known *a priori*. As shown in Fig. 4.9 and 4.10, the coupling of output signals then creates deviations of the load reflection coefficients, Γ_L , of all transmission path, i.e., load-pull. Complementary to the emulation technique, this chapter and Paper E introduce a technique to improve the precision of S-parameter measurements (a subset of transmission and reflection coefficients) and enables estimations of source and load reflection coefficients when the incident and reflected waves are non-sinusoidal wideband modulated signals.

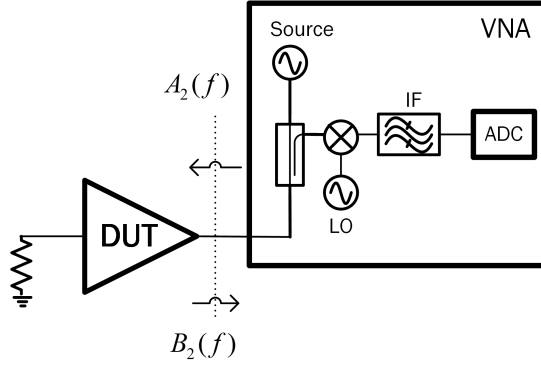


Figure 5.1. Simplified operation of a VNA when measuring S_{22} .

5.1.1 Vector Network Analyzers: S-Parameters

Vector network analyzers (VNA), simplified and shown in Fig. 5.1, are common instruments used to measure S-parameters of the device under test (DUT). Note that a VNA is a complex instrument [138], whose exact implementation can vary significantly; Fig. 5.1 is not included to address this point, but merely to facilitate the subsequent discussions.

A VNA operates by sweeping the frequency of a sinusoidal source injected at a port of the DUT, whose other ports are appropriately terminated. At a frequency point, the incident and reflected waves are then measured simultaneously by the RXs inside the VNA. The S-parameter can then be calculated as a function of the corresponding pair of incident and reflected waves. The VNA can be calibrated from prior standardized measurements which are nicely summarized in [139], the S-parameter at the plane of interest (represented by the dash-line) can then be obtained. The sinusoidal source is then swept to the next frequency point and the procedure repeats. The precision of such measurement is affected by noise at the RXs, which can be alleviated through the intermediate frequency (IF) filter. In such a measurement system, there is a fundamental trade-off between the precision of the measurement and the required measurement time. The trade-off exists in both the calibration stage and the measurement of the DUT. With a given number of frequency points, this trade-off is controlled by the IF bandwidth, typically variable, of the aforementioned RXs. With larger IF bandwidth, the measurement is quick but noisy, and hence, imprecise. A precise measurement typically requires lower IF bandwidths and longer measurement time. To illustrate, Fig. 5.2 shows measured S_{21} of a DUT at varying IF bandwidths. This constraint is exacerbated at mm-wave not only due to the wider measurement bandwidth, but also the higher loss of the test bench interconnects. Improvements to the precision and measurement time trade-off are therefore of significant and practical interests to wideband VNA measurements of mm-wave components.

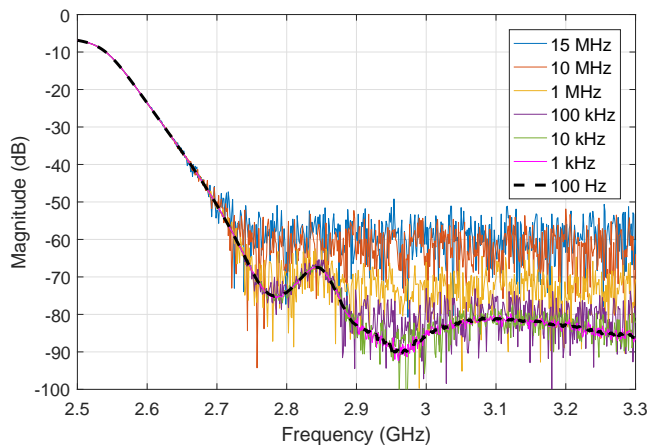


Figure 5.2. Measured S_{21} of a DUT at varying IF bandwidths of the VNA, from Paper E.

5.1.2 Active Load-Pull: Load Relection Coefficients

Active load-pull is a characterization measurement, first proposed by Takayama in 1976 for the open-loop variant [140] and Bava *et al.* in 1982 for the closed-loop variant [141]. In such measurement, the DUT is evaluated at different source and load terminations (reflection coefficients). The characterization could then offer information on the optimal terminations given the performance metrics. The varying terminations are created by the interactions between incident and reflected waves, typically sinusoidal, at the respective planes and must be controlled through a mechanism within the measurement environment. An overview of modern load-pull systems can be found in [21]. A simplified active load-pull setup is shown in Fig. 5.3.

Recently, there has been a surge of research interests in characterizations of the DUT under real usage scenarios: the technique proposed in Chapter 4 and Paper C is but one example. The benefit of such approach is well-recognized [142–145]. In these measurement systems, the incident and reflected waves are non-sinusoidal wideband modulated signals. Additionally, measurements have been reported to utilize the merits of such signals in various ways: Roblin *et al.* proposed an active load-pull system which uses modulated signals to improve measurement time [146]; while Thorsell *et al.* proposed a technique to generate time-varying terminations using modulated signals [147]. However, the estimation of the reflection coefficients created by the interactions of these non-sinusoidal signals is non-trivial. Furthermore, the estimation of the coefficients at low signal-to-noise ratio (SNR) frequency regions, e.g., intermodulation region, is not easily feasible. To demonstrate, Fig. 5.4 shows the estimated reflection coefficients in comparison to the trivial true values. The 3-dB and null-to-null bandwidths of the wideband incident and reflected waves are 10 MHz and 18 MHz, respectively. Similar to the S-parameter measurements, these constraints are further exacerbated at mm-wave frequencies due to the higher loss of test bench interconnects [148]. A technique to improve the

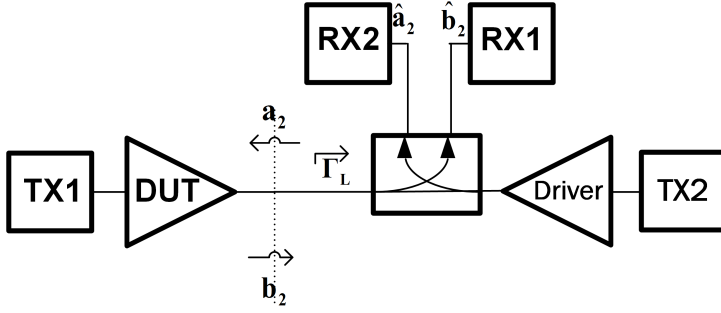


Figure 5.3. Simplified active load-pull setup, from Paper E.

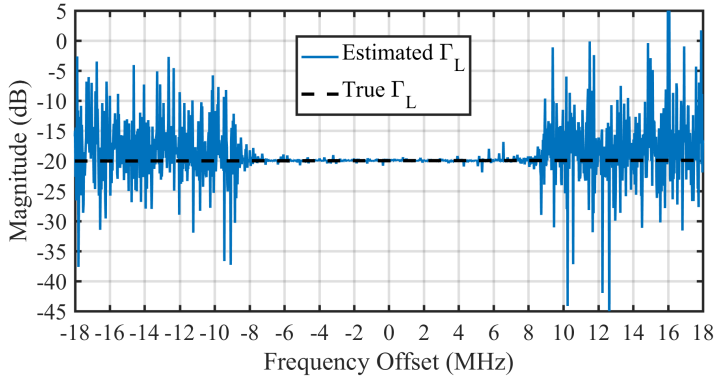


Figure 5.4. Estimated and true magnitudes of Γ_L as a function of frequency offset from the center frequency, modified from Paper CP4.

precision of reflection coefficients estimation in active load-pull and enables estimation of such coefficients in the low-SNR regions is therefore of practical interest.

5.2 Measurement

5.2.1 Setup (Framework)

The measurement systems of a VNA in Fig. 5.1 and an active load-pull test bench in Fig. 5.3 can be generalized to a generic measurement setup for a two-port DUT shown in Fig. 5.5. The setup consists of

1. a DUT to be characterized
2. two TXs to inject stimuli (sinusoidal or modulated signals)
3. two RXs to measure incident and reflected waves
4. two couplers and switches to select the pairing of incident and reflected waves

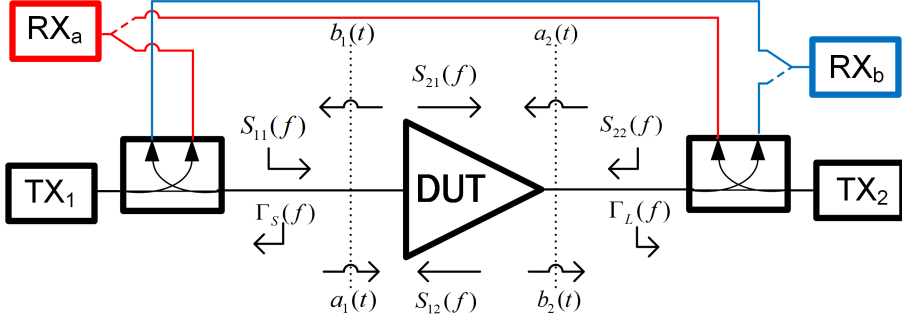


Figure 5.5. Generic measurement setup for a two-port DUT, from Paper E.

5. a mechanism to synchronize the timing of all components (not shown)

The extension of the setup to N -port device is trivial (conceptually) and will not be illustrated.

5.2.2 Definition-Based Approach

In Fig. 5.5, the transmission and reflection coefficients are also identified.

VNA S-parameter Measurements

Recalling (4.3) in Chapter 4: for an N -port DUT, a frequency-domain reflected wave at the k^{th} frequency-point and the i^{th} port, $B_i[k]$, is [149]

$$B_i[k] = \sum_{j=1}^N S_{ij}[k] A_j[k], \quad (5.1)$$

where $A_j[k]$ is the frequency-domain incident wave at the j^{th} port. $S_{ij}[k]$, is the S-parameter from port j to port i , which can be formulated as [149]

$$S_{ij}[k] = \frac{B_i[k]}{A_j[k]} : A_{\forall i \neq j}[k] = 0, \quad (5.2)$$

where it can be seen that S-parameter is either transmission or reflection coefficients with additional terminations condition. Equation (5.2) in vector form is

$$\mathbf{S}_{ij} = \frac{\mathbf{B}_i}{\mathbf{A}_j} : \mathbf{A}_{\forall i \neq j} = \mathbf{0}_K, \quad (5.3)$$

where \mathbf{S}_{ij} , \mathbf{B}_i , and \mathbf{A}_j are $K \times 1$ vectors with K being the number of measured frequency points. $\mathbf{0}_K$ is a $K \times 1$ zero-vector, and \div denotes element-wise division.

Define noise added at the two RXs: RX_a and RX_b (see Fig. 5.5), as \mathbf{W}_a and \mathbf{W}_b , respectively, such that

$$\mathbf{W}_a \sim \mathcal{N}(0, \sigma_w^2) \quad (5.4)$$

$$\mathbf{W}_b \sim \mathcal{N}(0, \sigma_w^2). \quad (5.5)$$

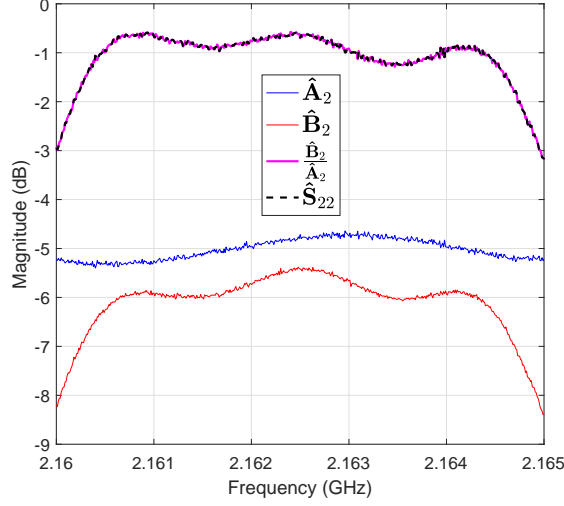


Figure 5.6. Comparison between the operation in (5.6) and VNA-measured $\hat{\mathbf{S}}_{22}$.

\mathbf{W}_a and \mathbf{W}_b are indepent and identically distributed (i.i.d.) zero-mean Gaussian random variables with variance of σ_w^2 . The measurable incident and reflected waves are $\hat{\mathbf{A}}_j$ and $\hat{\mathbf{B}}_i$, respectively. An estimation of $\tilde{\mathbf{S}}_{ij}$ based on its definition in (5.3) is then

$$\tilde{\mathbf{S}}_{ij} = \frac{\hat{\mathbf{B}}_i}{\hat{\mathbf{A}}_j} = \frac{\mathbf{B}_i + \mathbf{W}_b}{\mathbf{A}_j + \mathbf{W}_a} : \mathbf{A}_{\forall i \neq j} = \mathbf{0}_K. \quad (5.6)$$

In an ideal VNA measurement, the power of the stimulated incident wave is expected to be satisfactorily high. In such case, $\frac{\|\mathbf{A}_j\|^2}{\|\mathbf{W}_a\|^2} \gg 1$, and (5.6) is approximated to

$$\tilde{\mathbf{S}}_{ij} = \frac{\hat{\mathbf{B}}_i}{\hat{\mathbf{A}}_j} \approx \frac{\mathbf{B}_i + \mathbf{W}_b}{\mathbf{A}_j} = \mathbf{S}_{ij} + \frac{\mathbf{W}_b}{\mathbf{A}_j} : \mathbf{A}_{\forall i \neq j} = \mathbf{0}_K. \quad (5.7)$$

It can be observed that for each frequency point, the estimated S-parameter is

$$\tilde{S}_{ij}[k] \sim \mathcal{N}(S_{ij}[k], \frac{\sigma_w^2}{A_j^2[k]}). \quad (5.8)$$

If the incident and reflected waves are sinusoidal, the operation in (5.6) is trivial. To illustrate, a comparison between VNA-measured S-parameters and the operation of (5.6) is shown in Fig. 5.6.

Active Load-Pull Γ_L Measurements

The above procedure can be directly applied to the estimation of $\tilde{\mathbf{\Gamma}}_L$ (see Fig. 5.5) to obtain

$$\tilde{\mathbf{\Gamma}}_L = \frac{\hat{\mathbf{A}}_2}{\hat{\mathbf{B}}_2} = \frac{\mathbf{A}_2 + \mathbf{W}_a}{\mathbf{B}_2 + \mathbf{W}_b}. \quad (5.9)$$

If the reflected wave from the output of the DUT is sufficiently high in power, such that $\frac{\|\mathbf{B}_2\|^2}{\|\mathbf{W}_b\|^2} \gg 1$, (5.9) is approximated to

$$\tilde{\Gamma}_L = \frac{\hat{\mathbf{A}}_2}{\hat{\mathbf{B}}_2} \approx \frac{\mathbf{A}_2 + \mathbf{W}_a}{\mathbf{B}_2} = \Gamma_L + \frac{\mathbf{W}_a}{\mathbf{B}_2}. \quad (5.10)$$

It can be observed that for each frequency point, the estimated load reflection coefficient is

$$\tilde{\Gamma}_L[k] \sim \mathcal{N}(\Gamma_L[k], \frac{\sigma_w^2}{B_2^2[k]}). \quad (5.11)$$

Equations (5.8) and (5.11) illustrate the mechanism of this approach. Complete error analysis of the definite forms in (5.6) and (5.9) is presented in Section II-B of Paper E.

If wideband modulated signals were used to perform either of these measurements, the frequency-domain operations in (5.6) and (5.9) are not trivial. In such case, the measured wideband time-domain incident and reflected waves can be transformed to the frequency-domain by using Fast-Fourier Transform (FFT). However, this approach is not ideal due to the well-known problems associated with FFT operation on such waveforms: pseudo-aliasing, picket-fencing, and “leakage” [150, 151].

5.3 Finite Impulse Response Least-Squares Approach

To improve the precision of the estimation of reflection and transmission coefficients and in conjunction solve the issues when wideband modulated signals are used, Finite Impulse Response Least-Squares Estimation (FIR-LSE) is proposed. Three variants of FIR-LSE have been developed as follows:

- I: time-domain operation on time-domain measurements
- II: time-domain operation on frequency-domain measurements
- III: frequency-domain operation on frequency-domain measurements

Variants I and III are included in Paper E, where the former is shown to be suitable for estimations of Γ_L in active load-pull systems with wideband modulated signals, and the latter is proposed for estimations of \mathbf{S}_{ij} in S-parameter measurements with a VNA.

5.3.1 FIR-LSE Variant I (Time-Time)

This is the most straight-forward variant of FIR-LSE: the estimation operation is done in time-domain on the time-domain incident and reflected waves. For estimations of Γ_L , the procedure is shown in Fig. 5.7 as follows:

1. The measured time-domain reflected wave of length N_0 at the output of the DUT (the *forward* wave), $\hat{\mathbf{b}}_2$, is modelled as the input of a finite impulse response (FIR) filter¹.

¹ $\hat{\mathbf{b}}_2$ is an $N_0 \times 1$ vector of $\hat{b}_2[n]$, which is the time-domain sample of $b_2[n]$ impaired by noise added at the RX_b (see Fig. 5.5), $\mathbf{w}_b \sim \mathcal{N}(0, \sigma_w^2)$.

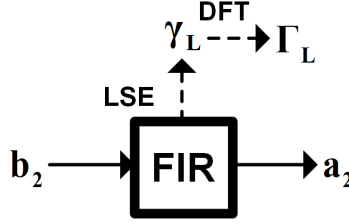


Figure 5.7. Simplified block diagram illustrating the mechanism of FIR-LSE (Variant I), from Paper E.

2. The measured time-domain incident wave of length N_0 at the output of the DUT (the *backward* wave), $\hat{\mathbf{a}}_2$, is modelled as the output of the aforementioned FIR filter².
3. Using an FIR filter model [152], the relationship between the ideal *forward* and *backward* waves is

$$a_2[n] = \sum_{m=0}^M \gamma_L[m] b_2[n - m], \quad (5.12)$$

where $\gamma_L[m]$ is the m^{th} filter coefficient of an M^{th} -order FIR filter. Denote $\bar{\gamma}_L$ as an $(M + 1) \times 1$ vector of $\gamma_L[m]$, the relationship between $\bar{\gamma}_L$ and Γ_L is

$$\Gamma_L = \mathbf{F} \bar{\gamma}_L, \quad (5.13)$$

where \mathbf{F} is the Discrete Fourier Transform (DFT) matrix. Equation (5.12) in vector form is

$$\mathbf{a}_2 = \mathbf{H}_L \bar{\gamma}_L. \quad (5.14)$$

\mathbf{H}_L is the time-domain observation $N_0 \times (M + 1) : M + 1 < N_0$ matrix such that

$$\mathbf{H}_L = \begin{bmatrix} \mathbf{h}_0 & \mathbf{h}_1 & \cdots & \mathbf{h}_M \end{bmatrix}, \quad (5.15)$$

where $\forall m \in \{0, 1, 2, \dots, M\}$,

$$\mathbf{h}_m = \begin{bmatrix} \mathbf{0}_m^T & b_2[0] & b_2[1] & \cdots & b_2[N_0 - (m + 1)] & b_2[N_0 - m] \end{bmatrix}^T. \quad (5.16)$$

\cdot^T is the transpose-operator. An intuitive description of (5.15) is that it represents an array of delay-lines of the FIR filter.

4. Cost function is imposed on the error of the measured *backward* wave, and least-squares (LS) estimation [153, 154] of $\tilde{\Gamma}_L$ is performed such that

$$\tilde{\Gamma}_L = \underset{\Gamma_L}{\operatorname{argmin}} \|\hat{\mathbf{a}}_2 - \mathbf{a}_2\|^2. \quad (5.17)$$

Applying (5.14) to (5.17) gives

$$\tilde{\Gamma}_L = \underset{\Gamma_L}{\operatorname{argmin}} \|\hat{\mathbf{a}}_2 - \mathbf{H}_L \bar{\gamma}_L\|^2, \quad (5.18)$$

² $\hat{\mathbf{a}}_2$ is an $N_0 \times 1$ vector of $\hat{a}_2[n]$, which is the time-domain sample of $a_2[n]$ impaired by noise added at the RX_a (see Fig. 5.5), $\mathbf{w}_a \sim \mathcal{N}(0, \sigma_w^2)$.

where (5.13) can be used to obtain

$$\tilde{\mathbf{\Gamma}}_L = \underset{\mathbf{\Gamma}_L}{\operatorname{argmin}} \left\| \hat{\mathbf{a}}_2 - \mathbf{H}_L \mathbf{F}^{-1} \mathbf{\Gamma}_L \right\|^2. \quad (5.19)$$

\cdot^{-1} is the inverse operator. By solving (5.19), the FIR-LSE estimated $\tilde{\mathbf{\Gamma}}_L$ is obtained:

$$\tilde{\mathbf{\Gamma}}_L = \mathbf{F} \hat{\mathbf{H}}_L^+ \hat{\mathbf{a}}_2, \quad (5.20)$$

where \cdot^+ is the pseudo-inverse. $\hat{\mathbf{H}}_L$ is \mathbf{H}_L in (5.15) but with the measured $\hat{\mathbf{b}}_2$.

To illustrate the efficacy of (5.20), the assumption in (5.10) (high SNR in the *forward* wave) is used such that $\hat{\mathbf{H}}_L \approx \mathbf{H}_L$. Consequently, (5.20) is approximated to

$$\tilde{\mathbf{\Gamma}}_L \approx \mathbf{\Gamma}_L + \mathbf{F} \mathbf{H}_L^+ \mathbf{w}_a. \quad (5.21)$$

Equation (5.21) shows the mechanism of FIR-LSE; coloring of the white noise.

5.3.2 FIR-LSE Variant II (Time-Frequency)

This variant is an *ad hoc* solution to utilize Variant I for estimations of S-parameter measured with a VNA. In such case, the frequency-domain vectors obtained from VNA measurements need to be converted to the time-domain. This is done by regenerating the superposition of sinusoids, a pseudo comb generator, with the corresponding frequency, magnitude, and phase. For the estimation of $\tilde{S}_{ij}[k]$, the incident wave is regenerated as

$$\hat{a}_j[n] = \sum_{k=0}^{K-1} \left| \hat{A}_j[k] \right| e^{j(2\pi n \frac{f[k]}{f_s} + \angle \hat{A}_j[k])}. \quad (5.22)$$

where j is $\sqrt{-1}$, $f[k]$ is the measurement frequency, and f_s is the prescribed sampling rate. To reduce the required sampling rate, $f[k]$ can be mapped to baseband frequencies. Likewise, the reflected wave is

$$\hat{b}_i[n] = \sum_{k=0}^{K-1} \left| \hat{B}_i[k] \right| e^{j(2\pi n \frac{f[k]}{f_s} + \angle \hat{B}_i[k])}. \quad (5.23)$$

The procedure described in Variant I then applies, where $\hat{\mathbf{a}}_i$ is modelled as the input of the FIR filter and $\hat{\mathbf{b}}_j$ as the output. From (5.20), the solution is

$$\tilde{S}_{ij} = \mathbf{F} \hat{\mathbf{H}}_{Sij}^+ \hat{\mathbf{b}}_i. \quad (5.24)$$

$\hat{\mathbf{H}}_{Sij}$ is \mathbf{H}_L in (5.15) but with the regenerated $\hat{\mathbf{a}}_j$ in (5.22).

The practicability of this variant is questionable due to the regenerations of the time-domain waveforms in (5.22) and (5.23) and the associated complexity. Further, the discussion here has so far ignored multiple parameters of the time-domain waveform generation which affect the performance of the FIR-LSE including the sampling rate and the length of the generated waveform.

Assuming uniform frequency spacing Δf of the measurement, the sampling rate and the length of the waveform must satisfy

$$\Delta f = f_{res,max} = I \times \frac{f_s}{N_0} = I \times f_{res} : I \in \mathbb{N}. \quad (5.25)$$

The sampling rate must also satisfy the Nyquist rate for baseband sampling. Fig. 5.8 illustrates the sensitivity of Variant II to these parameters. The estimation error (both magnitude and phase) is quantified through normalized mean-square error (NMSE) relative to the control values.

5.3.3 FIR-LSE Variant III (Frequency-Frequency)

Due to the inefficiency (and arguably the inefficacy) of Variant II; Variant III, which operates directly on frequency domain measurements, is developed.

To realize Variant III, which addresses the application in S-parameter measurements: the FIR model in (5.12) is modified such that the incident wave, $a_i[n]$, is the input to the FIR filter and the reflected wave, $b_j[n]$, is the output:

$$b_i[n] = \sum_{m=0}^M \gamma_{ij}[m] a_j[n-m]. \quad (5.26)$$

To obtain the frequency-domain operation, (5.26) is Fourier-transformed to obtain:

$$B_i[k] = A_j[k] \sum_{m=0}^M \gamma_{ij}[m] L_m[k] : L_m[k] = e^{-j2\pi m \frac{k}{K}}. \quad (5.27)$$

$L_m[k]$ is the k^{th} element of an $N_0 \times 1$ vector, \mathbf{L}_m , $\forall m \in \{0, 1, 2, \dots, M\}$. Equation (5.27) can be understood by considering the Fourier transform of time-delay in (2.23) in Chapter 2. Equation (5.27) assumes constant frequency spacing. Denote $\tilde{\gamma}_{ij}$ as an $(M+1) \times 1$ vector of $\gamma_{ij}[m]$, the relationship between $\tilde{\gamma}_{ij}$ and \mathbf{S}_{ij} is

$$\mathbf{S}_{ij} = \mathbf{F} \tilde{\gamma}_{ij}. \quad (5.28)$$

The vector-form of (5.27) is

$$\mathbf{B}_i = \mathbf{X}_{ij} \tilde{\gamma}_{ij}, \quad (5.29)$$

where \mathbf{X}_{ij} is an $N_0 \times (M+1) : M+1 < N_0$ frequency-domain observation matrix defined as

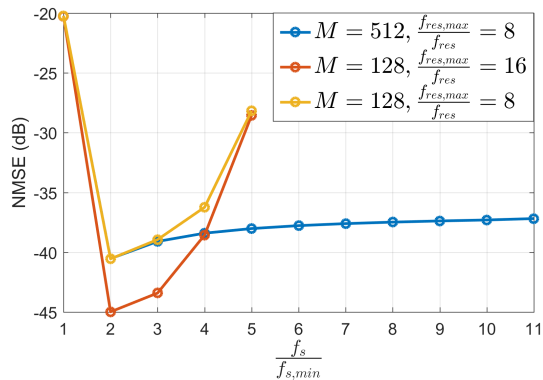
$$\mathbf{X}_{ij} = \begin{bmatrix} \mathbf{A}_j & \mathbf{A}_j \circ \mathbf{L}_1 & \mathbf{A}_j \circ \mathbf{L}_2 & \cdots & \mathbf{A}_j \circ \mathbf{L}_M \end{bmatrix}. \quad (5.30)$$

$\cdot \circ \cdot$ denotes element-wise multiplication. Imposing the cost function on the reflected wave and applying the LS estimator gives

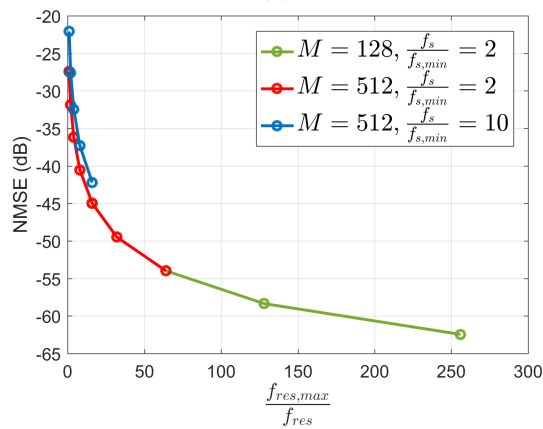
$$\tilde{\mathbf{S}}_{ij} = \underset{\mathbf{S}_{ij}}{\operatorname{argmin}} \left\| \hat{\mathbf{B}}_i - \mathbf{B}_i \right\|^2. \quad (5.31)$$

By using (5.28) and (5.29), (5.31) becomes

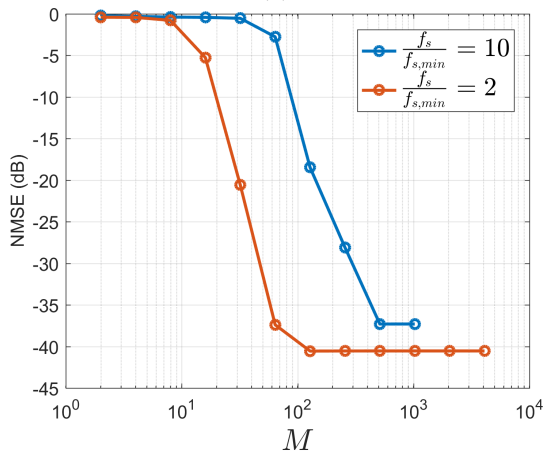
$$\tilde{\mathbf{S}}_{ij} = \underset{\mathbf{S}_{ij}}{\operatorname{argmin}} \left\| \hat{\mathbf{B}}_i - \mathbf{X}_{ij} \tilde{\gamma}_{ij} \right\|^2 = \underset{\mathbf{S}_{ij}}{\operatorname{argmin}} \left\| \hat{\mathbf{B}}_i - \mathbf{X}_{ij} \mathbf{F}^{-1} \mathbf{S}_{ij} \right\|^2. \quad (5.32)$$



(a)



(b)



(c)

Figure 5.8. Experimental illustration of the effects of FIR LSE (Variant II) parameters: (a) f_s , (b) f_{res} , and (c) M .

The solution of (5.32) is

$$\tilde{\mathbf{S}}_{ij} = \mathbf{F}\hat{\mathbf{X}}_{ij}^+\hat{\mathbf{B}}_i, \quad (5.33)$$

where $\hat{\mathbf{X}}_{ij}$ is \mathbf{X}_{ij} in (5.30) but with the measured $\hat{\mathbf{A}}_j$.

To illustrate the efficacy of Variant III, the assumption in (5.10) and (5.21) (high SNR of the input to the FIR filter model) is used such that $\hat{\mathbf{X}}_{ij} \approx \mathbf{X}_{ij}$. Consequently, (5.33) is approximated to

$$\tilde{\mathbf{S}}_{ij} \approx \mathbf{S}_{ij} + \mathbf{F}\mathbf{X}_{ij}^+\mathbf{W}_b. \quad (5.34)$$

Just as with Variant I, (5.34) shows the white noise coloring mechanism of FIR-LSE.

5.4 Applications

The efficacy of Variants I and III are thoroughly demonstrated in Paper E, where significant performance gain in precision has been experimentally demonstrated in both wideband active loadpull and S-parameter measurement applications. To summarize, the application of FIR-LSE is suitable in the following conditions:

1. The required order of the FIR filter is not excessively large.
2. The measurement has finite bandwidth.
3. Measurements of resonating structures assume finite number of modes [155].
4. If the incident and reflected waves are sinusoidal, both waveforms are not simultaneously ideal in terms of SNRs.

Chapter 6

Conclusions

This thesis has demonstrated the holistic development of mm-wave communication systems. The unified multi-disciplinary efforts, which consists of mm-wave circuits, sub-systems and system designs, characterization measurement techniques, and digital signal processing, have achieved the following key results:

1. Enhanced spectral efficiency using spectrally-efficient signals for mm-wave
2. A simple low-cost low-complexity architecture for mm-wave signal generations
3. New measurement technique to characterize components under mutual coupling effects
4. A frequency-domain measurement technique to improve the precision of fast S-parameter measurements
5. A new time-domain method enabling the estimations of load reflection coefficients in wideband active load-pull measurements

The main vision of this thesis is to create a new paradigm to solve challenging practical research problems found at mm-wave frequencies. Two research objectives have been addressed: realizations of efficient mm-wave data transmission and developments of measurement techniques enabling and assisting the design and evaluation of mm-wave circuits. To fulfill these, all elements of this thesis have been theoretically analyzed and experimentally demonstrated for their efficacies and efficiencies in real usage scenarios.

6.1 Contributions

The contents of the thesis and the appended papers are briefly summarized.

Chapter 2, Paper A, and Paper D have experimentally demonstrated the transmission of Spectrally Efficient Frequency Division Multiplexing (SEFDM) in dual polarization coherent optical system over 80 km and in mm-wave testbed at E-band. Techniques and impairment compensation algorithms were developed to mitigate various practical issues found in both systems. The optical

demonstration in Paper A laid the foundations for the successful demonstration at mm-wave in Paper D. Moreover, two variants of SEFDM were demonstrated: with decoder and with FEC. It has been shown that with standard existing error correction mechanism found in modern systems, SEFDM offers enhanced spectral efficiency relative to standard signals, while achieving satisfactory performance.

Chapter 3 and Paper B present a variant of multiplier-based transmitter architecture. The low-cost low-complexity approach is experimentally demonstrated to be suitable for generations of mm-wave signals using relatively large multiplication-factors. The nonlinear effects of the multiplier including severe bandwidth expansions are satisfactorily mitigated through a simple phase retarder predistorter. Impairment correction algorithms were also designed and implemented in the digital receiver to further enhance the overall performance of the system.

Chapter 4 and Paper C have proposed a new characterization measurement technique to evaluate the device under test under the effect of mutual coupling in antenna arrays. This allows components such as power amplifiers to be characterized in real usage scenarios at early design stages. The technique can emulate the coupling effects while requiring only one copy of the device under test to be realized, an attribute which saves cost and development time. Further, the technique can represent the transmission scenarios down to the characteristics of the signals found in various applications. The device under test can then be evaluated through system-level key performance indicators (KPIs) in addition to conventional metrics. These indicators include error-vector magnitude, adjacent channel power ratio, and even bit-error rate. Finally, the emulation technique does not require any construction of the actual array and does not contain any cumbersome mapping procedures between the measurement and the transmission environments. These qualities and attributes make the technique an appealing and viable tool enabling and assisting the designs of complex mm-wave architecture.

Chapter 5 and Paper E proposed a novel technique to measure reflection and transmission coefficients. Variants I and III of the technique are presented in Paper E while Variant II is included in Chapter 5. Variant III, which operates in the frequency-domain, is suitable for improving the precision of S-parameters measured with lower signal-to-noise ratios (SNR) in the reflected waves. The application of Variant III assists and supports measurements of mm-wave wideband components and systems. On the other hand, Variant I, which operates in the time-domain, was developed specifically to enable estimations of load-reflection coefficients in active load-pull measurements with wideband modulated signals, a non-trivial task with the standard approach. The application of Variant I enables and assists controlled active load pull measurements to be performed with signals found in real application scenarios, which then further enhances the specificity of the characterization and evaluation of the device.

6.2 Future Directions

The work in this thesis has laid the foundations for further development of the holistic paradigm of mm-wave systems. The existing objectives can be further extended as follows:

Efficient mm-wave data transmission

- **Additional dimension of spectral efficiency:** As shown in this thesis, SEFDM adds an additional dimension of continuously tunable spectral efficiency adjustment. Combination of SEFDM with other spectrally efficient technique such as Massive MIMO would yet add another dimension of spectral efficiency enhancement. This would result in a total of three dimensions of spectral efficiency adjustments: the symbol, the carrier, and the spatial domain. Such combination would provide challenging and rewarding practical research problems and new solutions will need to be developed.
- **Optimized spectral efficiency:** The tunable spectral efficiency of SEFDM can be used as an optimization parameter. Implementations of SEFDM in software-defined radios (SDR) for mm-wave transmissions could prove a worthwhile effort in this regard. The spectral efficiency of the transmission could then be tuned as the transmission environment allows.

Measurement techniques to enable and assist the design and evaluation of mm-wave circuits

- **New transmission environments:** This thesis has presented a measurement technique to evaluate the performance of a device under test in antenna array environments, e.g., beamforming and Massive MIMO scenarios. As transmission techniques continue to evolve, new transmission structures, mechanisms, and environments will present new sets of challenges. The development of measurement techniques to evaluate components under these new conditions and subsequently report relevant system level KPIs is an interesting research area. Further development of the emulation technique in Chapter 4 by utilizing the estimation technique in Chapter 5 is one viable approach.
- **Backward evaluation of circuits:** In this thesis, a technique was developed to evaluate and characterize the device under test in the *forward* direction, i.e., if the impairment is known what is the resulting effect on the KPIs. *Backward* evaluation, which identifies the impairments based on the available observations, is a challenging and interesting area to explore.
- **Identification of optimal FIR-LSE orders:** In Chapter 5 and Paper E, the orders of FIR-LSE were chosen manually. A method to identify the optimal order of FIR-LSE, e.g., based on characteristics of fast and noisy measurements, is a complementary practical component.

Acknowledgments

I am very proud to say that this thesis and its content may not have been possible without the support I have received throughout my PhD journey, which started on January 22, 2015. During this time, I have co-supervised three MSc theses and a BSc project to completion. I have assisted in the teaching of two MSc courses: Wireless Link Project as an instructor since 2015 and Wireless and Photonics System Engineering as a tutor since 2018. These would not have been possible without the opportunities and teamwork afforded to me by examiners and colleagues, which I deeply appreciate.

Even though a thesis represents the pinnacle of doctoral studies, the journey itself is multifaceted. In addition to research endeavors, teaching responsibilities and coursework accomplishments, I believe, are crucial elements to my personal development. In the spirit of the holistic approach, I would like to utilize these few pages to acknowledge not only the contributions of those involved from the research standpoint but the journey as a whole.

This journey is funded in part by the Swedish Foundation for Strategic Research.

First and foremost, I would like to express my sincere gratitude to my main supervisor, Prof. Herbert Zirath, for his mentorship and advice, both professionally and personally. Our “do you have a minute?” discussions are among the day-to-day things I really appreciate. Most importantly, thank you for providing me with the opportunity to pursue the paths that I believe in.

To my external supervisor, Prof. Izzat Darwazeh, who was my MSc dissertation supervisor and previous employer from the Dept. of Electronic and Electrical Engineering, University College London (UCL), for his continued support. Having had firsthand observations on how busy you are, I really appreciate all the visits you have made during the course of my PhD studies. Most importantly, thank you for always believing in me.

To Assistant Prof. Koen Buisman, who became a co-supervisor in 2018, for his advice and assistance: measurement-related and otherwise. Who would have thought an impromptu coffee-room discussion would start a chain of events which led to publications, an invited presentation, and more?

To co-supervisor, Assistant Prof. Zhongxia He, thank you for fruitful collaborations.

To Prof. Thomas Eriksson, who was a co-supervisor until 2018 and remained as an external supervisor from the Dept. of Electrical Engineering at Chalmers, for fruitful technical discussions and collaborations. Most importantly, thank

you for showing me DSP analytical approaches to problems and for recommending the two PhD courses on model-based signal processing and probability theory!

To the “boss” of Wireless Link Project, Associate Prof. Vessen Vassilev, for his friendship and continued support. Milena and your family have always made me feel welcome whenever I visited, and I truly appreciate that. Thanks again for helping me change my tyres, but please do not remember me as my car!

To Prof. Christian Fager, for his support and together with Prof. Magnus Karlsson for giving me the teaching opportunity in Wireless and Photonics System Engineering.

I wish to express my special gratitude to Dr. Marcus Gavell, Dr. Hedaia Ghannam of UCL, Assistant Prof. Omid Habibpour, and Dr. William Hallberg for the pleasant and fruitful research collaborations. Many thanks to Dr. Sebastian Gustafsson and Ahmed Adel Hassona for their support and for the fantastic teaching collaboration in Wireless Link Project. Thanks are also due to Henric Fjellstedt, Catharina Forssen, Debora Perlheden, and the team at MC2 for providing the excellent network of support at the lab and the department. Thanks to Marlene Bonmann and Xinxin Yang for accompanying me on this journey since 2015. To all former and current colleagues and friends on the 6th-floor; I apologize that I cannot name you all, but please know that I truly appreciate your friendship, support, and the wonderful environment you have created.

Finally, I wish to express my deepest gratitude and appreciation to my family and friends in Gothenburg, London, Bangkok, and elsewhere for making every day a joy.

*This work is dedicated to my parents,
Dr. Chattrin and Chorsaward Nopchinda.
Without whom, I would not be.*

“If I have seen further,
it is by standing upon the shoulders of giants.”

Isaac Newton, 1675.

Bibliography

- [1] Internet World Stats, “World Internet users and 2019 population stats,” 2019. [Online]. Available: <https://www.internetworldstats.com>
- [2] Population Division - United Nations, “World population prospects 2019,” 2019. [Online]. Available: <https://population.un.org>
- [3] Cisco, “Cisco Visual Networking Index: Forecast and trends, 2017–2022,” 2019. [Online]. Available: <https://www.cisco.com>
- [4] Sandvine, “The global Internet phenomena report,” 2018. [Online]. Available: <https://www.sandvine.com>
- [5] Z. Pi and F. Khan, “An introduction to millimeter-wave mobile broadband systems,” *IEEE Communications Magazine*, vol. 49, no. 6, pp. 101–107, Jun. 2011.
- [6] C. Dehos, J. González, A. Domenico, D. Kténas, and L. Dussopt, “Millimeter-wave access and backhauling: The solution to the exponential data traffic increase in 5G mobile communications systems?” *IEEE Communications Magazine*, vol. 52, no. 9, pp. 88–95, Sep. 2014.
- [7] P. Wang, Y. Li, L. Song, and B. Vucetic, “Multi-gigabit millimeter wave wireless communications for 5G: From fixed access to cellular networks,” *IEEE Communications Magazine*, vol. 53, no. 1, pp. 168–178, Jan. 2015.
- [8] G. Sellin, J. Edstam, A. Olsson, J. Flodin, M. Öhberg, A. Henriksson, J. Hansryd, J. Ahlberg, and I. Mikulic, “Ericsson microwave outlook,” Dec. 2018.
- [9] A. Hassona, Z. S. He, V. Vassilev, C. Mariotti, S. E. Gunnarsson, F. Dielacher, and H. Zirath, “Demonstration of +100-GHz interconnects in eWLB packaging technology,” *IEEE Transactions on Components, Packaging and Manufacturing Technology*, vol. 9, no. 7, pp. 1406–1414, Jan. 2019.
- [10] M. R. Khanzadi, D. Kuylenstierna, A. Panahi, T. Eriksson, and H. Zirath, “Calculation of the performance of communication systems from measured oscillator phase noise,” *IEEE Transactions on Circuits and Systems I: Regular Papers*, vol. 61, no. 5, pp. 1553–1565, Jan. 2014.

- [11] J. Antes and I. Kallfass, "Performance estimation for broadband multi-gigabit millimeter- and sub-millimeter-wave wireless communication links," *IEEE Transactions on Microwave Theory and Techniques*, vol. 63, no. 10, pp. 3288–3299, Sep. 2015.
- [12] J. Chen, D. Kuylenstierna, S. E. Gunnarsson, Z. S. He, T. Eriksson, T. Swahn, and H. Zirath, "Influence of white LO noise on wideband communication," *IEEE Transactions on Microwave Theory and Techniques*, vol. 66, no. 7, pp. 3349–3359, Mar. 2018.
- [13] ITU-R, "Attenuation by atmospheric gases and related effects," 2019.
- [14] M. R. D. Rodrigues and I. Darwazeh, "A spectrally efficient frequency division multiplexing based communication system," in *Proceedings of the 8th International OFDM-Workshop (InOWo'03)*, Hamburg, 2003, pp. 70–74.
- [15] I. Kanaras, A. Chorti, M. R. D. Rodrigues, and I. Darwazeh, "A fast constrained sphere decoder for ill conditioned communication systems," *IEEE Communications Letters*, vol. 14, no. 11, pp. 999–1001, Nov. 2010.
- [16] R. G. Gallager, "Low-density parity-check codes," *IRE Transactions on Information Theory*, vol. 8, no. 1, pp. 21–28, Jan. 1962.
- [17] 3GPP, "5G; study on new radio (NR) access technology (release 14)," The European Telecommunications Standards Institute, Tech. Rep., 2017.
- [18] M. Funabashi, T. Inoue, K. Ohata, K. Maruhashi, K. Hosoya, M. Kuzuhara, K. Kanekawa, and Y. Kobayashi, "A 60 GHz MMIC stabilized frequency source composed of a 30 GHz DRO and a doubler," in *Proceedings of 1995 IEEE MTT-S International Microwave Symposium*, Orlando, FL, 1995, pp. 71–74.
- [19] M. Abbasi, R. Kozhuharov, C. Karnfelt, I. Angelov, I. Kallfass, A. Leuther, and H. Zirath, "Single-chip frequency multiplier chains for millimeter-wave signal generation," *IEEE Transactions on Microwave Theory and Techniques*, vol. 57, no. 12, pp. 3134–3142, Dec. 2009.
- [20] J. W. Wallace and M. A. Jensen, "Mutual coupling in MIMO wireless systems: A rigorous network theory analysis," *IEEE Transactions on Wireless Communications*, vol. 3, no. 4, pp. 1317–1325, Jul. 2004.
- [21] A. Ferrero and M. Pirola, "Harmonic load-pull techniques: An overview of modern systems," *IEEE Microwave Magazine*, vol. 14, no. 4, pp. 116–123, Jun. 2013.
- [22] J. Choi, "On coding and beamforming for large antenna arrays in mm-wave systems," *IEEE Wireless Communications Letters*, vol. 3, no. 2, pp. 193–196, Apr. 2014.
- [23] R. Rajashekar and L. Hanzo, "Hybrid beamforming in mm-wave MIMO systems having a finite input alphabet," *IEEE Transactions on Communications*, vol. 64, no. 8, pp. 3337–3349, Aug. 2016.

- [24] P. Botsinis, D. Alanis, S. Feng, Z. Babar, H. V. Nguyen, D. Chandra, S. X. Ng, R. Zhang, and L. Hanzo, "Quantum-assisted indoor localization for uplink mm-wave and downlink visible light communication systems," *IEEE Access*, vol. 5, pp. 23 327–23 351, 2017.
- [25] Y. Cai, Y. Xu, Q. Shi, B. Champagne, and L. Hanzo, "Robust joint hybrid transceiver design for millimeter wave full-duplex MIMO relay systems," *IEEE Transactions on Wireless Communications*, vol. 18, no. 2, pp. 1199–1215, Feb. 2019.
- [26] A. Hirata, T. Kosugi, H. Takahashi, R. Yamaguchi, F. Nakajima, T. Furuta, H. Ito, H. Sugahara, Y. Sato, and T. Nagatsuma, "120-GHz-band millimeter-wave photonic wireless link for 10-Gb/s data transmission," *IEEE Transactions on Microwave Theory and Techniques*, vol. 54, no. 5, pp. 1937–1942, May 2006.
- [27] H. Takahashi, T. Kosugi, A. Hirata, J. Takeuchi, K. Murata, and N. Kukutsu, "120-GHz-band fully integrated wireless link using QSPK for realtime 10-Gbit/s transmission," *IEEE Transactions on Microwave Theory and Techniques*, vol. 61, no. 12, pp. 4745–4753, Dec. 2013.
- [28] C. Wang, C. Lin, Q. Chen, B. Lu, X. Deng, and J. Zhang, "A 10-Gbit/s wireless communication link using 16-QAM modulation in 140-GHz band," *IEEE Transactions on Microwave Theory and Techniques*, vol. 61, no. 7, pp. 2737–2746, Jul. 2013.
- [29] C. Wang, B. Lu, C. Lin, Q. Chen, L. Miao, X. Deng, and J. Zhang, "0.34-THz wireless link based on high-order modulation for future wireless local area network applications," *IEEE Transactions on Terahertz Science and Technology*, vol. 4, no. 1, pp. 75–85, Jan. 2014.
- [30] S. Carpenter, D. Nopchinda, M. Abbasi, Z. S. He, M. Bao, T. Eriksson, and H. Zirath, "A D-band 48-Gbit/s 64-QAM/QPSK direct-conversion I/Q transceiver chipset," *IEEE Transactions on Microwave Theory and Techniques*, vol. 64, no. 4, pp. 1285–1296, Apr. 2016.
- [31] K. Katayama, K. Takano, S. Amakawa, S. Hara, T. Yoshida, and M. Fujishima, "CMOS 300-GHz 64-QAM transmitter," in *IEEE MTT-S International Microwave Symposium Digest*, San Francisco, TX, 2016, pp. 1–4.
- [32] D. Fritsche, P. Starke, C. Carta, and F. Ellinger, "A low-power SiGe BiCMOS 190-GHz transceiver chipset with demonstrated data rates up to 50 Gbit/s using on-chip antennas," *IEEE Transactions on Microwave Theory and Techniques*, vol. 65, no. 9, pp. 3312–3323, Sep. 2017.
- [33] P. Rodriguez-Vazquez, J. Grzyb, B. Heinemann, and U. R. Pfeiffer, "A 16-QAM 100-Gb/s 1-m wireless link with an EVM of 17% at 230 GHz in an SiGe technology," *IEEE Microwave and Wireless Components Letters*, vol. 29, no. 4, pp. 297–299, Apr. 2019.
- [34] R. M. Santos and N. B. Carvalho, "EVM estimation in RF/wireless components," in *IEEE International Symposium on Personal, Indoor and Mobile Radio Communications (PIMRC)*, 2007, pp. 1–5.

- [35] H. Q. Ngo, E. G. Larsson, and T. L. Marzetta, "Energy and spectral efficiency of very large multiuser MIMO systems," *IEEE Transactions on Communications*, vol. 61, no. 4, pp. 1436–1449, Apr. 2013.
- [36] J. Bingham, "Multicarrier modulation for data transmission: An idea whose time has come," *IEEE Communications Magazine*, vol. 28, no. 5, pp. 5–14, May 1990.
- [37] R. W. Chang, "Synthesis of band-limited orthogonal signals for multichannel data transmission," *Bell System Technical Journal*, vol. 45, no. 10, pp. 1775–1796, Dec. 1966.
- [38] M. R. Perrett and I. Darwazeh, "Flexible hardware architecture of SEFDM transmitters with real-time non-orthogonal adjustment," in *2011 18th International Conference on Telecommunications*, Ayia Napa, 2011, pp. 369–374.
- [39] I. Kanaras, A. Chorti, M. R. D. Rodrigues, and I. Darwazeh, "Spectrally efficient FDM signals: Bandwidth gain at the expense of receiver complexity," in *2009 IEEE International Conference on Communications*, Dresden, 2009, pp. 1–6.
- [40] P. N. Whatmough, M. R. Perrett, S. Isam, and I. Darwazeh, "VLSI architecture for a reconfigurable spectrally efficient FDM baseband transmitter," in *2011 IEEE International Symposium of Circuits and Systems (ISCAS)*, Rio de Janeiro, 2011, pp. 1688–1691.
- [41] IEEE Standard 802.11a, "Part 11: Wireless LAN medium access control (MAC) and physical layer (PHY) specifications: High-speed physical layer in the 5 GHz band," 1999.
- [42] IEEE Standard 802.16a, "Local and metropolitan area networks—part 16, air interface for fixed broadband wireless access systems," 2009.
- [43] S. Weinstein and P. Ebert, "Data transmission by frequency-division multiplexing using the discrete Fourier transform," *IEEE Transactions on Communication Technology*, vol. 19, no. 5, pp. 628–634, Oct. 1971.
- [44] P. Moose, "A technique for orthogonal frequency division multiplexing frequency offset correction," *IEEE Transactions on Communications*, vol. 42, no. 10, pp. 2908–2914, Oct. 1994.
- [45] M. Alard and R. Halbert, "Principles of modulation and channel coding for digital broadcasting for mobile receivers," *EBU Review*, no. 224, pp. 168–190, Aug. 1987.
- [46] L. Deng, M. Beltran, X. Pang, X. Zhang, V. Arlunno, Y. Zhao, A. Caballero, A. Dogadaev, X. Yu, R. Llorente, D. Liu, and I. T. Monroy, "Fiber wireless transmission of 8.3-Gb/s/ch QPSK-OFDM signals in 75–110-GHz band," *IEEE Photonics Technology Letters*, vol. 24, no. 5, pp. 383–385, Mar. 2012.

- [47] F. Li, J. Yu, Z. Cao, J. Xiao, H. Chen, and L. Chen, "Reducing the peak-to-average power ratio with companding transform coding in 60 GHz OFDM-ROF systems," *Journal of Optical Communications and Networking*, vol. 4, no. 3, p. 202, Mar. 2012.
- [48] D. Qian, J. Yu, J. Hu, P. N. Ji, and T. Wang, "11.5-Gb/s OFDM transmission over 640 km SSMF using directly modulated laser," in *2008 34th European Conference on Optical Communication*, Brussels, 2008, pp. 53–54.
- [49] T. Xu and I. Darwazeh, "Spectrally efficient FDM: Spectrum saving technique for 5G?" in *Proceedings of the 1st International Conference on 5G for Ubiquitous Connectivity*, Levi, 2014, pp. 273–278.
- [50] S. Mikroulis, T. Xu, J. E. Mitchell, and I. Darwazeh, "First demonstration of a spectrally efficient FDM radio over fiber system topology for beyond 4G cellular networking," in *2015 20th European Conference on Networks and Optical Communications (NOC)*, London, 2015, pp. 1–5.
- [51] T. Xu, S. Mikroulis, J. E. Mitchell, and I. Darwazeh, "Bandwidth compressed waveform for 60-GHz millimeter-wave radio over fiber experiment," *Journal of Lightwave Technology*, vol. 34, no. 14, pp. 3458–3465, Jul. 2016.
- [52] H. Ghannam and I. Darwazeh, "Power allocation for detection performance enhancement of SEFDM signals," in *2018 IEEE 29th Annual International Symposium on Personal, Indoor, and Mobile Radio Communications (PIMRC)*, Bologna, Sep. 2018, pp. 584–585.
- [53] —, "Design and performance of SEFDM signals with power allocation," in *IEEE Proc. Wireless Communications and Networking Conference (WCNC)*, Marrakech, Apr. 2019.
- [54] I. Kanaras, A. Chorti, M. Rodrigues, and I. Darwazeh, "A combined MMSE-ML detection for a spectrally efficient non orthogonal FDM signal," in *2008 5th International Conference on Broadband Communications, Networks and Systems*, London, 2008, pp. 421–425.
- [55] —, "A new quasi-optimal detection algorithm for a non orthogonal spectrally efficient FDM," in *2009 9th International Symposium on Communications and Information Technology*, Icheon, 2009, pp. 460–465.
- [56] A. Chorti, I. Kanaras, M. R. Rodrigues, and I. Darwazeh, "Joint channel equalization and detection of spectrally efficient FDM signals," in *21st Annual IEEE International Symposium on Personal, Indoor and Mobile Radio Communications*, Istanbul, 2010, pp. 177–182.
- [57] T. Xu, R. C. Grammenos, F. Marvasti, and I. Darwazeh, "An improved fixed sphere decoder employing soft decision for the detection of non-orthogonal signals," *IEEE Communications Letters*, vol. 17, no. 10, pp. 1964–1967, Oct. 2013.

- [58] T. Xu and I. Darwazeh, "M-QAM signal detection for a non-orthogonal system using an improved fixed sphere decoder," in *2014 9th International Symposium on Communication Systems, Networks & Digital Sign (CSNDSP)*, Manchester, 2014, pp. 623–627.
- [59] —, "A soft detector for spectrally efficient systems with non-orthogonal overlapped sub-carriers," *IEEE Communications Letters*, vol. 18, no. 10, pp. 1847–1850, Oct. 2014.
- [60] S. Isam, I. Kanaras, and I. Darwazeh, "A truncated SVD approach for fixed complexity spectrally efficient FDM receivers," in *2011 IEEE Wireless Communications and Networking Conference*, Cancun, 2011, pp. 1584–1589.
- [61] R. C. Grammenos, S. Isam, and I. Darwazeh, "FPGA design of a truncated SVD based receiver for the detection of SEFDM signals," in *2011 IEEE 22nd International Symposium on Personal, Indoor and Mobile Radio Communications*, Toronto, 2011, pp. 2085–2090.
- [62] S. Isam and I. Darwazeh, "Design and performance assessment of fixed complexity spectrally efficient FDM receivers," in *2011 IEEE 73rd Vehicular Technology Conference (VTC Spring)*, Yokohama, 2011, pp. 1–5.
- [63] R. C. Grammenos and I. Darwazeh, "Hardware implementation of a practical complexity spectrally efficient FDM reconfigurable receiver," in *2012 IEEE 23rd International Symposium on Personal, Indoor and Mobile Radio Communications (PIMRC)*, Sydney, 2012, pp. 2401–2407.
- [64] M. R. Perrett, R. C. Grammenos, and I. Darwazeh, "A verification methodology for the detection of spectrally efficient FDM signals generated using reconfigurable hardware," in *2012 IEEE International Conference on Communications (ICC)*, Ottawa, ON, 2012, pp. 3686–3691.
- [65] T. Xu, R. C. Grammenos, and I. Darwazeh, "FPGA implementations of real-time detectors for a spectrally efficient FDM system," in *International Conference on Telecommunications (ICT 2013)*, Casablanca, 2013, pp. 1–5.
- [66] I. Darwazeh, T. Xu, T. Gui, Y. Bao, and Z. Li, "Optical SEFDM system; bandwidth saving using non-orthogonal sub-carriers," *IEEE Photonics Technology Letters*, vol. 26, no. 4, pp. 352–355, Feb. 2014.
- [67] U. Fincke and M. Pohst, "Improved methods for calculating vectors of short length in a lattice, including a complexity analysis," *Mathematics of Computation*, vol. 44, no. 170, pp. 463–471, Apr. 1985.
- [68] T. Cui and C. Tellambura, "An efficient generalized sphere decoder for rank-deficient MIMO systems," *IEEE Communications Letters*, vol. 9, no. 5, pp. 423–425, May 2005.
- [69] B. Hassibi and H. Vikalo, "On the expected complexity of integer least-squares problems," in *IEEE International Conference on Acoustics Speech and Signal Processing*, Orlando, FL, 2002, pp. 1497–1500.

- [70] —, “On the sphere-decoding algorithm I. expected complexity,” *IEEE Transactions on Signal Processing*, vol. 53, no. 8, pp. 2806–2818, Aug. 2005.
- [71] T. Xu and I. Darwazeh, “Transmission experiment of bandwidth compressed carrier aggregation in a realistic fading channel,” *IEEE Transactions on Vehicular Technology*, vol. 66, no. 5, pp. 4087–4097, May 2017.
- [72] H. Ghannam and I. Darwazeh, “Signal coding and interference cancellation of spectrally efficient FDM systems for 5G cellular networks,” in *Proceedings of the 24th International Conference on Telecommunications: Intelligence in Every Form, ICT 2017*, Limassol, 2017, pp. 1–6.
- [73] —, “SEFDM over satellite systems with advanced interference cancellation,” *IET Communications*, vol. 12, no. 1, pp. 59–66, Dec. 2018.
- [74] B. C. Thomsen, R. Maher, D. S. Millar, and S. J. Savory, “Burst mode receiver for 112 Gb/s DP-QPSK with parallel DSP,” *Optics Express*, vol. 19, no. 26, pp. 770–776, Dec. 2011.
- [75] R. Maher, D. S. Millar, S. Savory, and B. Thomsen, “Fast wavelength switching 112 Gb/s coherent burst mode transceiver for dynamic optical networks,” in *European Conference and Exhibition on Optical Communication*, Amsterdam, 2012, pp. 1–3.
- [76] A. J. Viterbi and A. M. Viterbi, “Nonlinear estimation of PSK-modulated carrier phase with application to burst digital transmission,” *IEEE Transactions on Information Theory*, vol. 29, no. 4, pp. 543–551, Jul. 1983.
- [77] E. Jacobsen and P. Kootsookos, “Fast, accurate frequency estimators [DSP tips & tricks],” *IEEE Signal Processing Magazine*, vol. 24, no. 3, pp. 123–125, May 2007.
- [78] F. Li, Z. Cao, X. Li, Z. Dong, and L. Chen, “Fiber-wireless transmission system of PDM-MIMO-OFDM at 100 GHz frequency,” *Journal of Lightwave Technology*, vol. 31, no. 14, pp. 2394–2399, Jul. 2013.
- [79] S. L. Jansen, I. Morita, T. C. Schenk, and H. Tanaka, “Long-haul transmission of 16×52.5 Gbits/s polarization-division-multiplexed OFDM enabled by MIMO processing (invited),” *Journal of Optical Networking*, vol. 7, no. 2, pp. 173–182, Feb. 2008.
- [80] T. Schmidl and D. Cox, “Robust frequency and timing synchronization for OFDM,” *IEEE Transactions on Communications*, vol. 45, no. 12, pp. 1613–1621, Dec. 1997.
- [81] I. Barhumi, G. Leus, and M. Moonen, “Optimal training design for MIMO OFDM systems in mobile wireless channels,” *IEEE Transactions on Signal Processing*, vol. 51, no. 6, pp. 1615–1624, Jun. 2003.
- [82] H. Ghannam and I. Darwazeh, “Robust channel estimation methods for spectrally efficient FDM systems,” in *IEEE Vehicular Technology Conference*, Porto, 2018, pp. 1–6.

- [83] S. L. Jansen, I. Morita, N. Takeda, and H. Tanaka, "20-Gb/s OFDM transmission over 4,160-km SSMF enabled by RF-pilot tone phase noise compensation," in *Optical Fiber Communication Conference*, Anaheim, CA, 2007, pp. 1–3.
- [84] S. Randel, S. Adhikari, and S. L. Jansen, "Analysis of RF-pilot-based phase noise compensation for coherent optical OFDM systems," *IEEE Photonics Technology Letters*, vol. 22, no. 17, pp. 1288–1290, Sep. 2010.
- [85] A. Chung, A. M. Darwish, E. Viveiros, H. A. Hung, P. Mitran, and S. Boumaiza, "Analysis and compensation of nonidealities in frequency multiplier-based high-frequency vector signal generators," *IEEE Transactions on Microwave Theory and Techniques*, vol. 67, no. 6, pp. 2270–2283, Jun. 2019.
- [86] J. H. Jeon, J. H. Choi, S. M. Kang, T. Y. Kim, W. Choi, and K. H. Koo, "A novel dual band transmitter for WLAN 802.11 a/g applications," in *2004 IEEE MTT-S International Microwave Symposium Digest*, Fort Worth, TX, 2004, pp. 1285–1288.
- [87] J. H. Choi, S. M. Kang, and K. H. Koo, "Digital predistortion of frequency multiplier for dual band wireless LAN transmitter," in *IEEE MTT-S International Microwave Symposium Digest*, Long Beach, CA, 2005, pp. 1999–2002.
- [88] Y. Park, R. Melville, R. Frye, M. Chen, and J. Kenney, "Dual-band transmitters using digitally predistorted frequency multipliers for reconfigurable radios," *IEEE Transactions on Microwave Theory and Techniques*, vol. 53, no. 1, pp. 115–122, Jan. 2005.
- [89] Y. Park, K. M. Low, and J. S. Kenney, "Digital predistortion linearization of frequency multipliers," in *IEEE MTT-S International Microwave Symposium Digest*, Philadelphia, PA, 2003, pp. 1695–1698.
- [90] Y. Park and J. S. Kenney, "Adaptive digital predistortion linearization of frequency multipliers," *IEEE Transactions on Microwave Theory and Techniques*, vol. 51, no. 12, pp. 2516–2522, Dec. 2003.
- [91] Y. Park, "Analysis on memory effects of frequency multipliers for the frequency translation of complex modulated signals," in *2007 Asia-Pacific Microwave Conference*, Bangkok, 2007, pp. 1–4.
- [92] Y. Liu, G. Liu, and P. M. Asbeck, "High-order modulation transmission through frequency quadrupler using digital predistortion," *IEEE Transactions on Microwave Theory and Techniques*, vol. 64, no. 6, pp. 1896–1910, Jun. 2016.
- [93] A. Chung, M. B. Rejeb, Y. Beltagy, A. M. Darwish, H. A. Hung, and S. Boumaiza, "High frequency and wideband modulated signal generation using frequency doublers," in *IEEE MTT-S International Microwave Symposium Digest*, Philadelphia, PA, 2018, pp. 156–159.

- [94] K. Katayama, K. Takano, S. Amakawa, S. Hara, A. Kasamatsu, K. Mizuno, K. Takahashi, T. Yoshida, and M. Fujishima, "A 300 GHz CMOS transmitter with 32-QAM 17.5 Gb/s/ch capability over six channels," *IEEE Journal of Solid-State Circuits*, vol. 51, no. 12, pp. 3037–3048, Dec. 2016.
- [95] J. Chen, Z. S. He, D. Kuylenstierna, T. Eriksson, M. Horberg, T. Emanuelsson, T. Swahn, and H. Zirath, "Does LO noise floor limit performance in multi-gigabit millimeter-wave communication?" *IEEE Microwave and Wireless Components Letters*, vol. 27, no. 8, pp. 769–771, Aug. 2017.
- [96] K. Takano, S. Hara, K. Katayama, S. Amakawa, T. Yoshida, and M. Fujishima, "Quintic mixer: A subharmonic up-conversion mixer for THz transmitter supporting complex digital modulation," in *2016 IEEE MTT-S International Microwave Symposium (IMS)*, San Francisco, CA, 2016, pp. 1–3.
- [97] K. Takano, S. Amakawa, K. Katayama, S. Hara, R. Dong, A. Kasamatsu, I. Hosako, K. Mizuno, K. Takahashi, T. Yoshida, and M. Fujishima, "A 105 Gb/s 300 GHz CMOS transmitter," in *IEEE International Solid-State Circuits Conference*, San Francisco, CA, 2017, pp. 308–400.
- [98] S. Gunnarsson, C. Karnfelt, H. Zirath, R. Kozhuharov, D. Kuylenstierna, A. Alping, and C. Fager, "Highly integrated 60 GHz transmitter and receiver MMICs in a GaAs pHEMT technology," *IEEE Journal of Solid-State Circuits*, vol. 40, no. 11, pp. 2174–2186, Nov. 2005.
- [99] H. Zirath, T. Masuda, R. Kozhuharov, and M. Ferndahl, "Development of 60-GHz front-end circuits for a high-data-rate communication system," *IEEE Journal of Solid-State Circuits*, vol. 39, no. 10, pp. 1640–1649, Oct. 2004.
- [100] S. Gunnarsson, C. Karnfelt, H. Zirath, R. Kozhuharov, D. Kuylenstierna, C. Fager, and A. Alping, "Single-chip 60 GHz transmitter and receiver MMICs in a GaAs mHEMT technology," in *2006 IEEE MTT-S International Microwave Symposium Digest*, San Francisco, CA, 2006, pp. 801–804.
- [101] C. Marcu, D. Chowdhury, C. Thakkar, J.-D. Park, L.-K. Kong, M. Tabesh, Y. Wang, B. Afshar, A. Gupta, A. Arbabian, S. Gambini, R. Zamani, E. Alon, and A. M. Niknejad, "A 90 nm CMOS low-power 60 GHz transceiver with integrated baseband circuitry," *IEEE Journal of Solid-State Circuits*, vol. 44, no. 12, pp. 3434–3447, Dec. 2009.
- [102] M. Abbasi, S. E. Gunnarsson, N. Wade Falk, R. Kozhuharov, J. Svedin, S. Cherednichenko, I. Angelov, I. Kallfass, A. Leuther, and H. Zirath, "Single-chip 220-GHz active heterodyne receiver and transmitter MMICs with on-chip integrated antenna," *IEEE Transactions on Microwave Theory and Techniques*, vol. 59, no. 2, pp. 466–478, Feb. 2011.

- [103] S. Kang, S. V. Thyagarajan, and A. M. Niknejad, "A 240 GHz fully integrated wideband QPSK transmitter in 65 nm CMOS," *IEEE Journal of Solid-State Circuits*, vol. 50, no. 10, pp. 2256–2267, Oct. 2015.
- [104] L. Ding and G. Zhou, "Effects of even-order nonlinear terms on power amplifier modeling and predistortion linearization," *IEEE Transactions on Vehicular Technology*, vol. 53, no. 1, pp. 156–162, Jan. 2004.
- [105] R. Parsons and S. Wilson, "Polar quantizing for coded PSK transmission," *IEEE Transactions on Communications*, vol. 38, no. 9, pp. 1511–1519, Sep. 1990.
- [106] F. Boccardi, R. Heath, A. Lozano, T. Marzetta, and P. Popovski, "Five disruptive technology directions for 5G," *IEEE Communications Magazine*, vol. 52, no. 2, pp. 74–80, Feb. 2014.
- [107] J. G. Andrews, S. Buzzi, W. Choi, S. V. Hanly, A. Lozano, A. C. K. Soong, and J. C. Zhang, "What will 5G be?" *IEEE Journal on Selected Areas in Communications*, vol. 32, no. 6, pp. 1065–1082, Jun. 2014.
- [108] N. Chiurtu, B. Rimoldi, and E. Telatar, "On the capacity of multi-antenna Gaussian channels," in *2001 IEEE International Symposium on Information Theory*, Washington, DC, 2001, p. 53.
- [109] M. Romier, A. Barka, H. Aubert, J. P. Martinaud, and M. Soiron, "Load-pull effect on radiation characteristics of active antennas," *IEEE Antennas and Wireless Propagation Letters*, vol. 7, pp. 550–552, Sep. 2008.
- [110] C. Fager, X. Bland, K. Hausmair, J. Chani Cahuana, and T. Eriksson, "Prediction of smart antenna transmitter characteristics using a new behavioral modeling approach," in *2014 IEEE MTT-S International Microwave Symposium (IMS 2014)*, Tampa, FL, 2014, pp. 1–4.
- [111] M. J. Al-Hasan, T. A. Denidni, and A. R. Sebak, "Mllimeter-wave hybrid isolator for mutual-coupling reduction applications," in *2014 16th International Symposium on Antenna Technology and Applied Electromagnetics (ANTEM)*, Victoria, 2014, pp. 1–2.
- [112] C. Shepard, H. Yu, N. Anand, L. E. Li, T. Marzetta, R. Yang, and L. Zhong, "Argos: Practical many-antenna base stations," in *MobiCom'12*, Istanbul, Aug. 2012, pp. 53–64.
- [113] J. Vieira, S. Malkowsky, K. Nieman, Z. Miers, N. Kundargi, L. Liu, I. Wong, V. Owall, O. Edfors, and F. Tufvesson, "A flexible 100-antenna testbed for Massive MIMO," in *2014 IEEE Globecom Workshops*, Austin, TX, 2014, pp. 287–293.
- [114] P. Harris, S. Zang, A. Nix, M. Beach, S. Armour, and A. Doufexi, "A distributed massive MIMO testbed to assess real-world performance and feasibility," in *IEEE Vehicular Technology Conference*, Glasgow, 2015, pp. 1–2.

- [115] S. Malkowsky, J. Vieira, L. Liu, P. Harris, K. Nieman, N. Kundargi, I. C. Wong, F. Tufvesson, V. Owall, and O. Edfors, "The world's first real-time testbed for Massive MIMO: Design, implementation, and validation," *IEEE Access*, vol. 5, pp. 9073–9088, 2017.
- [116] K. Buisman and T. Eriksson, "Designing and characterizing MATE, the Chalmers mm-wave MIMO testbed," in *12th European Conference on Antennas and Propagation (EuCAP 2018)*, London, UK, Apr. 2018.
- [117] S. Farsi, J. Dooley, K. Finnerty, D. Schreurs, B. Nauwelaers, and R. Farrell, "Behavioral modeling approach for array of amplifiers in active antenna array system," in *2013 IEEE Topical Conference on Power Amplifiers for Wireless and Radio Applications*, Santa Clara, CA, 2013, pp. 73–75.
- [118] K. Hausmair, S. Gustafsson, C. Sanchez-Perez, P. N. Landin, U. Gustavsson, T. Eriksson, and C. Fager, "Prediction of nonlinear distortion in wideband active antenna arrays," *IEEE Transactions on Microwave Theory and Techniques*, vol. 65, no. 11, pp. 4550–4563, Nov. 2017.
- [119] K. Hausmair, P. N. Landin, U. Gustavsson, C. Fager, and T. Eriksson, "Digital predistortion for multi-antenna transmitters affected by antenna crosstalk," *IEEE Transactions on Microwave Theory and Techniques*, vol. 66, no. 3, pp. 1524–1535, Mar. 2018.
- [120] R. M. Foster, "Directive diagrams of antenna arrays," *Bell System Technical Journal*, vol. 5, no. 2, pp. 292–307, Apr. 1926.
- [121] A. Bailey, S. Dean, and W. Wintringham, "The receiving system for long-wave trans-Atlantic radio telephony," *Proceedings of the IRE*, vol. 16, no. 12, pp. 1645–1705, Dec. 1928.
- [122] J. Schelleng, "Some problems in short-wave telephone transmission," *Proceedings of the IRE*, vol. 18, no. 6, pp. 913–938, Jun. 1930.
- [123] G. Southworth, "Certain factors affecting the gain of directive antennas," *Proceedings of the IRE*, vol. 18, no. 9, pp. 1502–1536, Sep. 1930.
- [124] S. G. Brown, "British patent no. 14419," 1899.
- [125] J. S. Stone, "United States patent no. 716131," 1901.
- [126] A. Blondel, "Belgian patent no. 163516," 1902.
- [127] E. G. Larsson, O. Edfors, F. Tufvesson, and T. L. Marzetta, "Massive MIMO for next generation wireless systems," *IEEE Communications Magazine*, vol. 52, no. 2, pp. 186–195, Feb. 2014.
- [128] A. J. Paulraj, D. A. Gore, R. U. Nabar, and H. Bölcskei, "An overview of MIMO communications — a key to gigabit wireless," *Proceedings of the IEEE*, vol. 92, no. 2, pp. 198–217, Feb. 2004.
- [129] J. Kim and K. Konstantinou, "Digital predistortion of wideband signals based on power amplifier model with memory," *Electronics Letters*, vol. 37, no. 23, p. 1417, Jun. 2001.

- [130] L. Ding, G. Zhou, D. Morgan, Z. Ma, J. Kenney, J. Kim, and C. Giardina, "A robust digital baseband predistorter constructed using memory polynomials," *IEEE Transactions on Communications*, vol. 52, no. 1, pp. 159–165, Jan. 2004.
- [131] D. Morgan, Z. Ma, J. Kim, M. Zierdt, and J. Pastalan, "A generalized memory polynomial model for digital predistortion of RF power amplifiers," *IEEE Transactions on Signal Processing*, vol. 54, no. 10, pp. 3852–3860, Oct. 2006.
- [132] C. Eun and E. Powers, "A new Volterra predistorter based on the indirect learning architecture," *IEEE Transactions on Signal Processing*, vol. 45, no. 1, pp. 223–227, Jan. 1997.
- [133] J. Chani-Cahuana, C. Fager, and T. Eriksson, "A new variant of the indirect learning architecture for the linearization of power amplifiers," in *2015 European Microwave Conference (EuMC)*, Paris, 2015, pp. 1295–1298.
- [134] A. Ferrero and U. Pisani, "Two-port network analyzer calibration using an unknown 'thru'," *IEEE Microwave and Guided Wave Letters*, vol. 2, no. 12, pp. 505–507, Dec. 1992.
- [135] —, "An improved calibration technique for on-wafer large-signal transistor characterization," *IEEE Transactions on Instrumentation and Measurement*, vol. 42, no. 2, pp. 360–364, Apr. 1993.
- [136] D. Gunyan and Y.-P. Teoh, "Characterization of active harmonic phase standard with improved characteristics for nonlinear vector network analyzer calibration," in *71st ARFTG Microwave Measurement Conference*, Atlanta, GA, 2008, pp. 1–7.
- [137] R. Benjamin, "On the use of delays for wide-band superdirective beam forming in endfire and broadside arrays," *The Radio and Electronic Engineer*, vol. 45, no. 9, pp. 451–461, Sep. 1975.
- [138] D. Rytting, "Network analyzer error models and calibration methods," 1998.
- [139] J. T. Barr and M. J. Pervere, "A generalized vector network analyzer calibration technique," in *34th ARFTG Conference Digest*, Ft. Lauderdale, FL, Dec. 1989, pp. 51–60.
- [140] Y. Takayama, "A new load-pull characterization method for microwave power transistors," in *IEEE MTT-S International Microwave Symposium*, Cherry Hill, NJ, Jun. 1976, pp. 218–220.
- [141] G. P. Bava, U. Pisani, and V. Pozzolo, "Active load technique for load-pull characterisation at microwave frequencies," *Electronics Letters*, vol. 18, no. 4, pp. 178–180, Feb. 1982.
- [142] H. Arthaber, M. L. Mayer, and G. Magerl, "A broadband active harmonic load-pull setup with a modulated generator as active load," in *European Microwave Conference*, Amsterdam, 2004, pp. 685–688.

- [143] M. Marchetti, M. J. Pelk, K. Buisman, W. C. Neo, M. Spirito, and L. C. De Vreede, "Active harmonic load-pull with realistic wideband communications signals," *IEEE Transactions on Microwave Theory and Techniques*, vol. 56, no. 12, pp. 2979–2988, Dec. 2008.
- [144] M. Marchetti, R. Heeres, M. Squillante, M. Pelk, M. Spirito, and L. C. De Vreede, "A mixed-signal load-pull system for base-station applications," in *IEEE Radio Frequency Integrated Circuits Symposium*, Anaheim, CA, 2010, pp. 491–494.
- [145] L. Galatro, M. Marchetti, and M. Spirito, "60 GHz mixed signal active load-pull system for millimeter wave devices characterization," in *80th ARFTG Microwave Measurement Conference: Advances in Wireless Communications Test and Measurements*, San Diego, CA, 2012, pp. 1–6.
- [146] P. Roblin, S. J. Doo, X. Cui, G. H. Jessen, D. Chaillot, and J. Strahler, "New ultra-fast real-time active load-pull measurements for high speed RF power amplifier design," in *IEEE MTT-S International Microwave Symposium Digest*, 2007, pp. 1493–1496.
- [147] M. Thorsell, K. Andersson, and C. Fager, "Characterization setup for device level dynamic load modulation measurements," in *IEEE MTT-S International Microwave Symposium Digest*, Boston, MA, 2009, pp. 1197–1200.
- [148] L. Galatro, A. Akhnoukh, P. Magnée, M. Marchetti, and M. Spirito, "Large signal characterization of millimeter wave devices using mixed signal active load-pull," in *82nd ARFTG Microwave Measurement Conference: Characterization, Modeling, and Design of RF and mm-Wave Devices and Circuits*, Columbus, OH, 2013.
- [149] N. Boulejfen, A. Ferrero, F. M. Ghannouchi, and A. B. Kouki, "An automated N-port network analyzer for linear and non linear multi-port RF and digital circuits," in *IEEE Instrumentation and Measurement Technology Conference*, Ottawa, 1997, pp. 36–39.
- [150] G. D. Bergland, "A guided tour of the fast Fourier transform," *IEEE Spectrum*, vol. 6, no. 7, pp. 41–52, Jul. 1969.
- [151] A. A. Girgis and F. M. Ham, "A quantitative study of pitfalls in the FFT," *IEEE Transactions on Aerospace and Electronic Systems*, vol. 16, no. 4, pp. 434–439, Jul. 1980.
- [152] L. R. Rabiner, B. Gold, and C. A. McGonegal, "An approach to the approximation problem for nonrecursive digital filters," *IEEE Transactions on Audio and Electroacoustics*, vol. 18, no. 2, pp. 83–106, Jun. 1970.
- [153] S. M. Kay, *Fundamentals of Statistical Signal Processing: Estimation Theory*, vol. 1. Upper Saddle River, NJ: Prentice Hall, 1993.
- [154] L. Ljung, *System Identification: Theory for the User*, 2nd ed. Upper Saddle River, NJ: Prentice Hall, 1999.

- [155] M. K. Zinn, “Network representation of transcendental impedance functions,” *Bell System Technical Journal*, vol. 31, no. 2, pp. 378–404, Mar. 1952.